



UNIVERSIDAD DE INVESTIGACIÓN DE TECNOLOGÍA EXPERIMENTAL YACHAY

Escuela de Ciencias Físicas y Nanotecnología

Comparative study of in situ multiwalled carbon nanotubes synthesis over metal substrate for harvesting the solar energy to be used at the industry

Trabajo de integración curricular presentado como requisito para
la obtención del título de Físico/a.

Autor:

Pico Vela Jorge Salvador

Tutor:

Reinoso Jerez Carlos Alberto, Ph.D.

Co – Tutor:

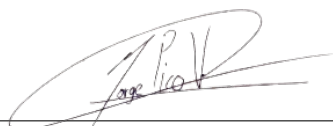
Corredor González Luis Gerardo
Escorza Cóndor Jonathan Lisandro

Urcuquí, mayo 2024

AUTORÍA

Yo, **Pico Vela Jorge Salvador**, con cédula de identidad 1727396309, declaro que las ideas, juicios, valoraciones, interpretaciones, consultas bibliográficas, definiciones y conceptualizaciones expuestas en el presente trabajo; así como, los procedimientos y herramientas utilizadas en la investigación, son de absoluta responsabilidad de el/la autora (a) del trabajo de integración curricular. Así mismo, me acojo a los reglamentos internos de la Universidad de Investigación de Tecnología Experimental Yachay.

Urcuquí, mayo 2024

A handwritten signature in black ink, appearing to read 'Jorge Pico Vela', is written over a horizontal line.

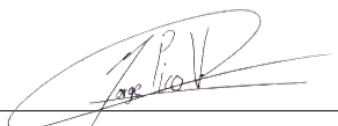
Jorge Salvador Pico Vela
CI: 1727396309

AUTORIZACIÓN DE PUBLICACIÓN

Yo, **Pico Vela Jorge Salvador**, con cédula de identidad 1727396309, cedo a la Universidad de Investigación de Tecnología Experimental Yachay, los derechos de publicación de la presente obra, sin que deba haber un reconocimiento económico por este concepto. Declaro además que el texto del presente trabajo de titulación no podrá ser cedido a ninguna empresa editorial para su publicación u otros fines, sin contar previamente con la autorización escrita de la Universidad.

Asimismo, autorizo a la Universidad que realice la digitalización y publicación de este trabajo de integración curricular en el repositorio virtual, de conformidad a lo dispuesto en el Art. 144 de la Ley Orgánica de Educación Superior.

Urququí, mayo 2024



Jorge Salvador Pico Vela

CI: 1727396309

Acknowledgements

The Ecuadorian education system has provided me the opportunity to expand my knowledge and professional background, while at the same time providing me with opportunities to learn from and of amazing people. I want to thank the professors, technicians, and overall staff of Yachay for the infinite knowledge the University has provided me, not only in science but also in the principles and values that are attached to this profession. Especial thanks to Carlos Reinoso, Gema Gonzalez, Julio Chacon, Mario Cosenza, and Henry Pinto, professors who gave me my career perspective, scientists who made me realize the beauty of nature, and humans who made this effort possible. This journey filled with science was also the opportunity to meet important people in my life. Humans that became my family through this journey: Daniela Osorio, Leonel Cabrera, Monse Ayala, Diana Ramos, Alejandro Vallejo and Andres Villares. You've helped me grow and brought me up when I needed to, I hope I can do the same for you.

To Emilio Paspuel and Emilia Hidalgo, we have known each other since day one and I'm sure I wouldn't be the same person I am today without you. Since we were assigned to the same apartment Emilio and I became friends and now I see you as my brother, you've helped me without any hesitation and you should know I would do the same. Emilia, I still remember when I saw you shaking on the first night in Yachay, and for some reason, I needed to approach and offer you my jacket, since then we grew together to be who we are right now. I know we wouldn't agree in everything, but my affection for you would always be greater than any problem. This thesis was written thanks to you. I'm so proud of you, you'll always be in my heart.

Thank you to my high school teachers who enabled me to begin this journey with solid bases for science and life, and trusted in my abilities: my math teacher Ec. Paul Cabezas, my chemistry teacher Ing. Marxia Suarez, the principal Doc. Ramiro Jaramillo and especially Ing. Pablo Alvarez, the one who opened up the world of physics for me and never doubted me as he was the proudest when I was admitted to Yachay.

Perhaps the most important part of my life is my family. Every thought, skill, and value I now have is thanks to their love and care. Thanks to my sisters Sofia and Maria Jose for being my confidants and my role models and thanks to my mom Soraya and my dad Jorge, watching you live has been a roadmap of how a human should behave, you are everything to me. And thanks to my whole family, my grandparents, María Eugenia and Washington, and Piedad and Jorge. My aunt Nathalie for your everlasting care since I was a child and all of my relatives. As I said in the beginning, you are the most important part of my life.

Lastly, to all the people that enabled this work to become a reality. Luis Corredor, Jonathan Escorza, and Johanna Pilicita from Yachay Tech thank you for your time, patience, and knowledge, and Dra. Yolanda Angulo, ESPE for letting science establish bonds between universities to create science for Ecuador. Thanks to every political and nonpolitical actor that resulted in the creation of Yachay, I was able to experience firsthand the future of science in Ecuador Thank you and I hope to contribute so everyone can see how bright this university shines.

Dedication

To my family, the light of my life.

In honor of Ing. Pablo Alvarez, the one who opened my eyes.

Resumen

Este estudio explora la aplicación de nanoestructuras de carbono, especialmente nanotubos que tienen muchas aplicaciones notables en varios campos de la ingeniería, para crear un material extremadamente absorbente de una amplia gama de radiación solar y convertirla en calor para fines industriales. Este trabajo demuestra un método novedoso de síntesis de MWCNTs (Nanotubos de Carbono de Pared Múltiple) cultivados por CVD (Deposición Química de Vapor) utilizando cobre y aluminio activados en superficie con sonicación y grabado electroquímico. La síntesis se realizó a 750 °C para el cobre y a 524 °C para el aluminio, y la caracterización del material verificó la existencia de MWCNTs con bandas características G, D y 2D ubicadas en 1346, 1582 y 2692 cm⁻¹, respectivamente. Las imágenes SEM revelaron la modificación superficial de las muestras metálicas y la presencia de MWCNTs con un rango de diámetro de 30 nm a 110 nm. El análisis XPS confirmó la presencia de enlaces de carbono sp² y sp³ asociados con los CNTs y varias formas de carbono amorfo. Por último, durante las pruebas de captura de calor, el material mostró una diferencia de 1 °C con las muestras no tratadas bajo la lámpara de Xenón y una diferencia aún mayor de 3.5 °C bajo la luz solar. Los resultados de intensidad luminosa mostraron que el material reflejaba 0.36 cd de la luz, alcanzando una propiedad ultra-negra, y el análisis de exergía de la muestra proporciona resultados prometedores para usos industriales a gran escala. Este trabajo de investigación tiene como objetivo abrir diferentes posibilidades para una transición parcial hacia la energía renovable en las industrias ecuatorianas utilizando el sol en un futuro cercano.

Keywords: MWCNTS, CVD, Raman , XPS, Energy, Heat, Exergy.

Abstract

This study explores the application of carbon nanostructures, especially nanotubes which have many remarkable applications in various fields of engineering, to create an extremely high absorbant material of wide range solar radiation and convert it into heat for industrial purposes. This work demonstrates a novel method of CVD-grown MWCNT synthesis using surface-activated copper and aluminum with sonication and electrochemical etching. The synthesis was done at 750 °C for copper and 524 °C for aluminum and the characterization of the material verified the existence of MWCNTs with G, D, and 2D characteristic bands located at 1346, 1582, and 2692 cm^{-1} correspondingly. SEM images revealed the surface modification of the metallic samples and the presence of MWCNTs with a diameter range from 30 nm to 110 nm. XPS analysis confirmed the presence of sp² and sp³ carbon bonds associated with CNTs and various amorphous carbon forms. Lastly during heat capture testing the material showed a 1 °C difference with non-treated samples under the Xenon lamp and an even wider difference of 3.5 °C under sunlight. Luminous intensity results showed that the material reflected 0.36 cd of the light, reaching an ultra-black property and exergy analysis of the sample provides promising results for scaled-up industrial uses. This research work aims to open up different possibilities for partial renewable energy transition in Ecuadorian industries using the sun in the near future.

Keywords: MWCNTS, CVD, Raman , XPS, Energy, Heat, Exergy.

Contents

List of Figures	xvii
List of Tables	xxi
1 Introduction	1
1.1 Industrial use of thermal energy	1
1.2 Green energy sources	2
1.3 Sun as a source of heat energy and heat capture	3
1.3.1 Sun as a source of heat	3
1.3.2 Heat capture and solar collectors	4
1.4 Problem Statement	5
1.5 General and Specific Objectives	5
1.5.1 General objective	5
1.5.2 Specific objectives	6
2 Theoretical & experimental background	7
2.1 Theoretical background	7
2.1.1 Black Body physics	7
2.2 Carbon Nanotubes (CNTs)	9
2.2.1 Double-walled and Multi-walled carbon nanotubes	9
2.2.2 Thermal properties of CNTs	10
2.2.3 Thermodynamics and exergy analysis	11
2.2.4 Experimental background	13
2.2.5 Surface pre-treatment for CVD	14
2.3 Characterization techniques	15
3 Methodology	19
3.1 Surface treatment	19
3.1.1 Mechanical Methods & Chemical Methods	19

3.1.2	Catalyst deposition	21
3.1.3	Synthesis of CNTs using CVD	22
3.1.4	CNTs characterization	22
3.1.5	Measuring heat capture of CNT-grown metallic surfaces	22
3.1.6	Temperature measuring setup	23
3.1.7	Solar Simulation Chamber (Xenon lamp)	25
4	Results & Discussion	29
4.1	Short Results Section 1 Heading for Table of Contents	29
4.1.1	Surface activation/etching	30
4.2	CNT growth over copper and aluminum using CVD.	34
4.3	Scanning Electron Microscopy (SEM) characterization of CNTs	35
4.4	Raman Spectroscopy of CNT-Al/-Cu	37
4.5	XPS analysis of the samples	39
4.6	Radiation capture results	42
4.7	Exergy analysis	44
4.8	Luminance results.	45
5	Conclusions & Outlook	47
5.1	Synthesis of CNTs over surface treated aluminum and copper	47
5.2	Characterization of MWCNTs	48
5.3	Radiation-thermal capture analysis.	48
5.4	Exergy of the samples	48
5.5	Luminance analysis	48
5.6	Outlook	49
A	Baseline removal	51
	Bibliography	53

List of Figures

1.1	Total primary energy consumption in Ecuador by fuel type 2021. Adapted Figure from ¹	2
1.2	Renewable heat consumption projection by type, 2007-2024. Modified Figure from ²	3
1.3	Types of solar collectors. Modified Figure from ³	5
2.1	CNTs with different chirality based on the indexes n and m. Computer generated images using Materials Studio	10
2.2	SWCNT and MWCNT from different perspectives. Computer generated images using Materials Studio	10
2.3	Thermal conductivity as a function of defect concentration. Figure from ⁴	11
2.4	(a) CVD reaction process inside the quartz tube. Modified Figure ⁵ (b) CVD basic instrument schematic.	14
2.5	a) Schematic diagram of a scanning electron microscope. Modified Figure from ⁶ b) Illustration of signals generated by the electron beam-specimen interaction in the scanning electron microscope. c) High magnification SEM (25kV) of luminal surface decorated with 3 nm Au/Pb film	18
3.1	Summary of the methodology used in the synthesis of CNTs over metallic plates. (a) Schematic of the treatments used during the synthesis. (b) Evolution of Al samples for each step of the synthesis.	19
3.2	Experimental setup schematic for electrochemical etching	20
3.3	Surface treatment of samples. (a) Aluminum after sonication in NaCl solution for 60 min. (b) Copper after sonication in NaCl solution for 60 min. (c) Copper sample during electrochemical etching.	21
3.4	Calibration setup. Four sensors submerged on ice water with two reference instruments in order to calculate the offset in each sensor.	23
3.5	Sensor calibration setup. Four sensors and two reference instrument submerged on ice water.	24
3.6	(a) Minolta Xs-100A luminance and color meter. (b) Left: DT-5808 Digital Multimeter and right: Boeco Digital Thermo-Hygrometer & Clock. Two reference instruments for calibration of the sensors.	25
3.7	Solar chamber heat capture test of the samples and luminometer setup.	26
3.8	CNT-Al, CNT-Cu, etched aluminium and etched copper under the light of the Xenon lamp to measure heat capture.	27

4.1	Copper and aluminum surfaces after surface treatment. Images obtained with optical microscopy and SEM. Description on Table 4.1	29
4.2	Pristine metallic plates under 25x optical microscopy. (a) Aluminum. (b) Copper.	30
4.3	Aluminum surfaces after sonication and chemical etching. Image done with optical microscope 50x. (a) Surface after sonication in NaCl for 30 min. (b) Surface after chemical etching. (c) Surface after sonication in NaCl for 60 min. (d) Surface after sonication in NaCl for 60 min and chemical etching.	31
4.4	Copper surfaces after chemical etching. Image done with optical microscope 50x. (a) Sample after 30 min of sonication in NaCl. (b) Sample after chemical etching. (c) Sample after 60 min of sonication. (d) Sample after sonication in NaCl for 60 min and chemical etching.	32
4.5	SEM of aluminum samples after sonication with 10% wt NaCl for 60 min and electrochemical etching using 10% wt H_2PO_4 as electrolyte with 8 V, 2A for 5 min . a) SEM MAG: 6.67 kx. b) SEM MAG: 100 kx.	33
4.6	SEM of copper samples after sonication with 10% wt NaCl for 60 min and electrochemical etching using 10% wt H_2PO_4 as electrolyte with 8 V, 2A for 5 min . a) SEM MAG: 6.67 kx. b) SEM MAG: 100 kx	33
4.7	Evolution of the metallic samples after 1) Polishing 2) Surface treatment 3) Catalyst deposition and 4) CVD synthesis.	34
4.8	CNT -Al and CNT-Cu samples after 15 and 20 min of reaction time in CVD.	35
4.9	SEM images of CNT-Al with a) SEM MAG: 500kx b) SEM MAG: 300kx	36
4.10	SEM images of CNT-Cu with a) SEM MAG: 300kx b) SEM MAG: 500kx	36
4.11	Raman spectra of three zones (Al1, Al2, Al3) of CNT grown over aluminum using Fe-Co catalyst with a reaction time of 15 min (Left) and 20 min (Right). Laser 532 nm.	37
4.12	Raman spectra of three zones (Cu1, Cu2, Cu3) of CNT grown over copper using Fe-Co catalyst with a reaction time of 15 min (Left) and 20 min (Right) Laser 532 nm.	37
4.13	Lorentzian curve fitting for CNT-Al sample. Calculations and baseline removal made in Python.	38
4.14	Lorentzian curve fitting for CNT-Cu sample. Calculations and baseline removal made in Python.	39
4.15	CNT-Al and CNT-Cu samples loaded into XPS sample holder	40
4.16	XPS survey spectra of (a)Al and (b)Cu samples after surface treatment (surface activation) and CVD reaction.	40
4.17	High resolution XPS C1s core level deconvoluted into main binding energy for (a) Al-CNT sample and (b) Cu-CNT sample.	41
4.18	High resolution XPS O1s core level deconvoluted into main binding energy for (a) Al-CNT sample and (b) Cu-CNT sample.. . . .	42
4.19	Calibration with offset and reference instruments for all the pt100 temperature sensors.	42
4.20	Temperature readings of the heat capture for 1)Al-CNT 2)Cu-CNT 3)Al 4)Cu under a xenon lamp.	43
4.21	Temperature readings of the heat capture for 1) Al-CNT 2) Cu-CNT 3) Al 4) Cu under the sun.	44
4.22	Temperature readings of the heat capture for 1) Al-CNT 2) Cu-CNT 3) Al 4) Cu under the sun.	44

4.23 Exergy available due to difference in temperature between CNT-Al, CNT-Cu, Al and Cu samples for: (a) test under Xenon lamp (b) test under sunlight 1 (c) test under sunlight 2. 45

A.1 Baseline removal using Baseline.py library for python. (a) shows the different baseline removals able for the spectra and (b) is the result after the removal for CNT-Al sample. (c) shows the different baseline removals able for the spectra and (d) is the result after the removal for CNT-Cu sample. . . 52

List of Tables

1.1	Table of solar water heating applications in the industry . Modified table from ⁷	4
2.1	Reported CVD production parameters taking into account catalyst and product. Adapted table from ^{8,9} .	13
2.2	Properties of the various Raman features in graphite and SWCNTs. Mode frequencies for dispersive modes are given at $E_L = 2.41$ eV. The term $d\omega/dE_L$ denotes the change of the phonon frequency in cm^{-1} produced by changing the laser energy by 1eV. Modified Table ¹⁰	17
3.1	Synthesis parameters used for CVD reaction in order to grow CNTs over Al and Cu surfaces.	22
4.1	Description of the results shown in Figure 4.1 for each sample	30

Chapter 1

Introduction

1.1 Industrial use of thermal energy

Energy is a key resource for social and economical progress of any nation. Usage of this resource at an industrial level represents about 37% of world's energy consumption for a wide range of activities in manufacturing, agriculture, mining and construction.¹¹

In relation to global energy consumption, heat is the majority form of consumption and approximately 50% of the heat generated is destined for industry. This heat contributes 40% to the global value of carbon dioxide CO_2 emissions from the burning of fossil fuels for its production. The burning of hydrocarbons mostly maintains the demand for heat, while renewable sources only supply 10% to 12% of global consumption.¹²

Approximately 86% of renewable energy in the industry comes from bioenergy, mainly in producing sectors with a large amount of biomass waste, such as sugar mills, paper producers, and agricultural sectors for export. IEA projections indicate a contribution of 8.9 EJ in 2018 to 10 EJ in 2024, however, these would cover only 9% of the global demand for industrial heat.¹ Industrial processes such as water heating, ventilation systems, ovens, greenhouses, drying systems, desalination, and refrigeration are systems dependent on heat energy. However, Norton illustrates how the energy source of these processes can be substituted or compensated with solar energy. The levels and potential for integration at the supply level have been reported by Vajen et al. at the level of Germany, Europe, and worldwide. In Ecuador, small and large-scale industrial processes require a heat supply.¹³

Currently, solar heat for industrial processes is almost negligible, constituting 0.02% of global consumption. However, these processes continue to grow for a limited market. During 2018, systems were created that cover approximately 37.6 MWh, increasing global capacity by 7% in the year.²

The demand for energy can be divided into three categories: electricity, low-temperature heat applications, and high-temperature industrial process heat. Electricity accounts for approximately 17% of the global final energy demand, while low-temperature heat applications account for 44%, and high-temperature industrial process heat accounts for 10%. Solar energy has been used for a long time in the residential building sector, but it is also well-suited for the industrial and manufacturing sectors due to the high volume of energy required for process heating

systems. For instance, processes such as drying, cleaning, washing, water heating, pasteurization, sterilization, and food processing require significant amounts of heat. The temperature level required for these industrial processes is similar, being below 250°C for almost all applications.¹

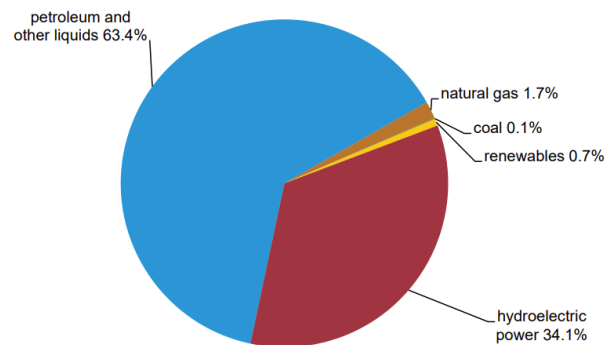


Figure 1.1: Total primary energy consumption in Ecuador by fuel type 2021. Adapted Figure from¹

1.2 Green energy sources

Green energy sources are increasingly recognized as crucial components of sustainable development. The use of renewable energy resources, such as solar, wind, and biomass, is advantageous because their availability will not diminish with use. Sunlight, a constant source of energy, is used to meet the ever-increasing energy demand.

Despite serious efforts to reduce reliance on fossil fuels by promoting renewable energy as an alternative, fossil fuels accounted for 73.5% of worldwide electricity production in 2017, while renewable sources contributed only 26.5%. The lack of public awareness is a major barrier to the acceptance of renewable energy technologies.¹⁴

The greatest sustainability challenge facing humanity today is greenhouse gas emissions and global climate change, with fossil fuels contributing 61.3% of global electricity generation in 2020. Sustainable energy transition strategies propose a roadmap for sustainable electricity generation and supply in line with the commitments of the Paris Agreement. These strategies typically involve energy savings on the demand side, generation efficiency at the production level, and the substitution of fossil fuels with various renewable energy sources.²

In conclusion, transitioning towards green energy sources is not only environmentally beneficial but also aligns with global efforts to mitigate climate change. However, this transition requires new technology to maximize the use of abundant but intermittent renewable sources. It also requires policy initiatives to guide the global electricity transition towards a sustainable energy and electricity system.

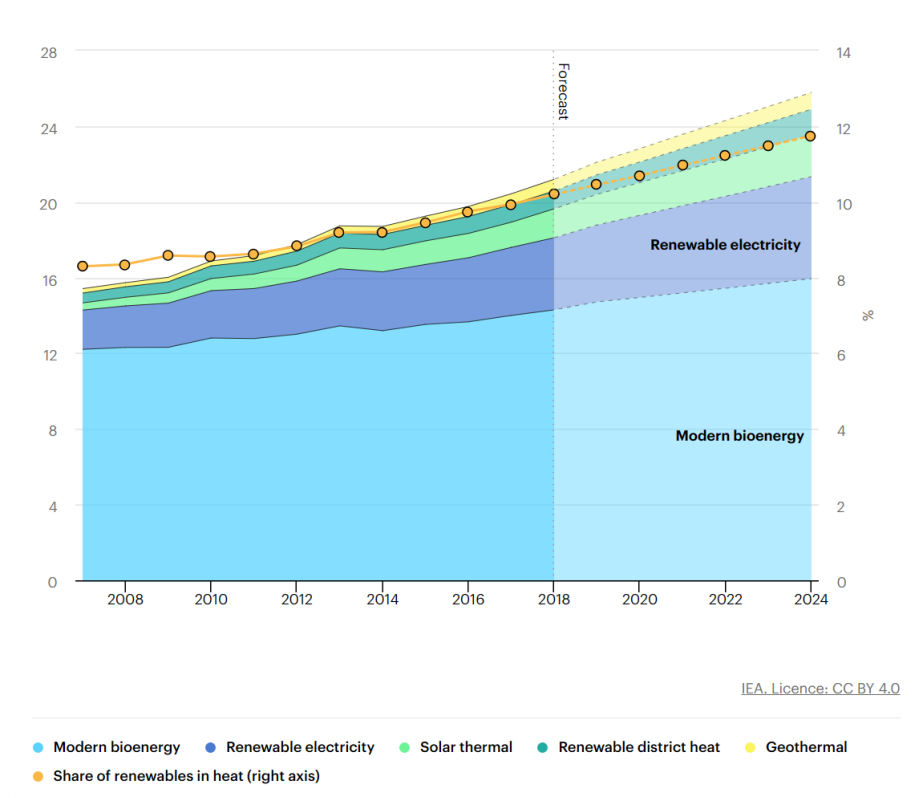


Figure 1.2: Renewable heat consumption projection by type, 2007-2024. Modified Figure from²

1.3 Sun as a source of heat energy and heat capture

1.3.1 Sun as a source of heat

The use of heat is essential to most industrial processes. Industries ranging from food to technology have specific steps where reaching a certain temperature is key for many steps of fabrication, refinement or treatment of products. Adding the necessity for green energy sources, solar heat becomes a valuable option for a transition to sustainable energy being a renewable and abundant source. This also aligns with the desire of countries throughout the world to industrialize their economy.³

Solar thermal energy (STE) is, in simple terms, the energy from the heat conversion gained from solar irradiation. The solar energy as any renewable energy has the potential to replace fossil fuels in industrial processes, however by itself has an evident problem. This type of energy cannot be supplied 24 hours a day and to overcome this problem, as reported by Shahjadi et. al.¹² supplementary process heating systems could be equipped using phase change materials or molten salts.

Several operations within an industrial process are already dependant on solar thermal heating. Water heating is

Industry	Country	Name	Industrial Operation	Solar Collector	Temperature(°C)	
Automobile	South Africa	BMW Manufacturing	Paint application process	Evacuated tube collector	-90	
Breweries	USA	Milwaukee Brewing Co.	Consumption	Flat plate collector		
	Germany	Hutt Brewery	Heating the brewing water	Flat plate collector	40-95	
Food	China	Chongqing Beverage	Heating for warehouse	Evacuated tube collector		
	Saudi Arabia	Nestle Waters	Bottle washing	Flat plate collector		
	Mexico	Aviary Food Pellet El Paisa	Heating water	Parallel trough collector	-95	
	Greece	Alpino S.A.	Hot water preheating in steam boiler	Flat plate collector	20-70	
			Cleaning equipment	Other or various collectors	20-90	
	Austria	Futtermittel Fruit Juice	Makeup water	Flat plate collector		
		Moguntia Spice Making	Cleaning and production process	Flat plate collector		
	Portugal	Knovee Best Foods S.A.	Tools washing	Flat plate collector	40-45	
	Spain	Montesano-canary islands	Wash meat derivatives	Flat plate collector	40-60	
	Czech Republic	PETA Bohemia Pekarna Sobeslav	Bakery	Flat plate collector	10-90	
Netherlands	Perfetti van melk	Preheating of hot water and process heat	Flat plate collector			
Textile	Jordan	Seniora Food Industries	Degreasing & cleaning requirements	Evacuated tube collector		
	USA	Acme McCrary	Textile drying process	Flat plate collector		
	Greece	Allegro S.A. Childrens' clothing manufacturer	Washing machines	Flat plate collector	33-60	
Mining	China	Daly Textile	Dyeing machines	Flat plate collector	40-90	
			Dyeing process	Flat plate collector	-55	
Chemical	India	Schiffer Gmbh & Co KG	Dyeing, bleaching & washing garments	Flat plate collector	-100	
			Galvanic baths	Evacuated tube collector	40-70	
Agriculture	Germany	Steinbach und Vallmann	Galvanic baths	Evacuated tube collector	60-80	
			Cleaning process	Flat plate collector	-55	
Leather	Spain	L'oreal Punne	Heating Water	Flat plate collector	23-26	
			Acuinova Andaluca S.A.	Water Heating	Evacuated tube collector	
			Hongxin Aquaculture	Water Heating	Parallel trough collector	
Fabricated Metal	Germany	Wulow	The wet process of leather retanning	Flat plate collector		
			Gerberei Kolblinger	Parallel trough collector	-95	
Wearing Apparel	India	SKF Technologies Mysore	Circulation	Flat plate collector		
			Chelsea Jeans	Parallel trough collector	-160	
Computer, electronic & optical products	Sweden	Bosmans Lackering	Dyeing process	Flat plate collector		
			Chemical baths	Parallel trough collector		
Machinery	Austria	Hoval Marchtrenk	Powder coating	Flat plate collector		
			Kral Pump Factory	Space heating	Evacuated tube collector	

Table 1.1: Table of solar water heating applications in the industry . Modified table from ⁷

a process where an integration of solar energy system presents a lot of advantages like energy and cost effectiveness and its applied on a large variety of process which can be seen in table 1.1 . This application of STE constitutes the major part of the industrial solar thermal applications.⁷

1.3.2 Heat capture and solar collectors

Solar collectors are devices that use a specific material to capture solar radiation and increase its temperature.¹⁵ Then, this material transfers the heat to the desired system. The type of solar collector determines how well it can absorb solar energy. There are two main types of solar collectors: stationary and tracking, as shown in Figure 1.3 . Stationary collectors include flat plate collectors, vacuum tube collectors with or without CPC5. Tracking collectors include parabolic, linear Fresnel, and concentrating dish collectors. The main difference between them is the temperature range, with stationary collectors working for low and medium temperatures (below 150 °C) and tracking collectors working for high temperatures (from 150 to 400 °C or more). Both types of collectors are designed to capture the shorter wavelengths of solar radiation (0.3 - 2 μm) and to minimize heat loss by infrared radiation. Solar collectors have been around since the 1760s, but they have not changed much in terms of materials and operation principles. This may be because the industrial sector is reluctant to invest in new technologies due to the high cost and risk involved. As a result, old and conventional technologies are still used and the transition to cleaner and sustainable energies is slow. Therefore, this work proposes a different kind of material to improve the solar radiation absorption and conversion into heat.¹⁵

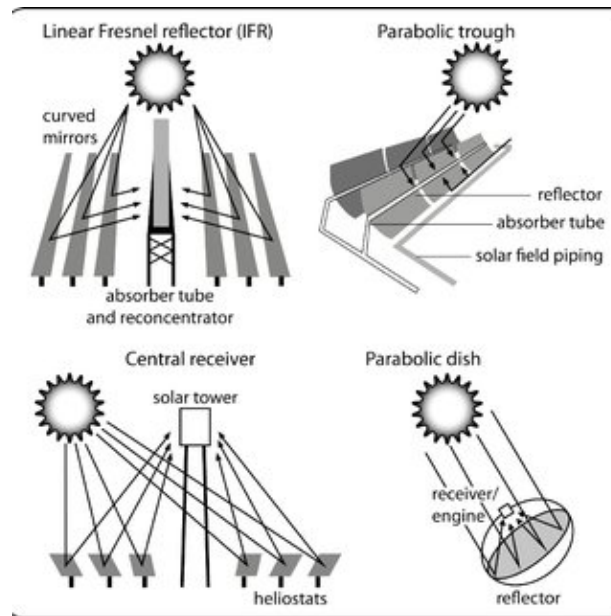


Figure 1.3: Types of solar collectors. Modified Figure from³

1.4 Problem Statement

The aim of this investigation is to find an optimal way to harvest solar energy by using copper and aluminum substrates where CNTs are grown using CVD methods. This way we take advantage of the absorption properties of CNTs and the conductivity of the metal. This investigation will cover the synthesis from a superficial treatment of the metal using mechanical and chemical methods next the growth in situ of multiwalled carbon nanotubes and lastly the characterization of the material synthesized and a comparative study of the absorptance to find the most efficient device.

1.5 General and Specific Objectives

1.5.1 General objective

Harvesting solar energy through Carbon nanotubes synthesized over a conductive metal to take advantage of the heat. Create a contribution to alternatives for renewable energy transitions using a solar absorber material able to transform solar radiation into heat for industrial processes. The basis of this material is CVD grown multi wall carbon nanotubes over copper and aluminum after a surface activation treatment.

1.5.2 Specific objectives

- Modify the surface of metallic substrates through mechanical and electrochemical etching in order to functionalize the substrate and enhance the catalyst deposition and synthesis quality.
- Synthesize a solar collector material based on multi wall carbon nanotubes over a surface-activated copper and aluminum substrates.
- Determine properties of the structure for the synthesized material through Raman microscopy, SEM and XPS.
- Create a device able to measure temperature simultaneously of metallic samples with high accuracy.
- Evaluate the efficiency of the produced material (CNT-Al and CNT-Cu) to capture heat under Xenon lamp radiation and sunlight.
- Execute an exergy analysis of the samples to identify the efficiency as solar absorber for industrial use.

Chapter 2

Theoretical & experimental background

To produce a material or device for radiation absorption properties we need to understand what characteristics are necessary for a material to be approximated to an ideal black-body. The idea of a black body is a theoretical object that absorb radiation in all frequencies and avoiding reflections. In the case of this work, a black body approximation is achieved by synthesising a CNT forest, trapping incoming radiation and enabling a process of absorption/excitation in which some it can convert into heat (phonons) into the substrate. Thus, this work stands on the background of both theoretical and experimental knowledge to create this device. In the theoretical section we will review the physical principles for the blackbody absorption as well as the characteristics CNTs have to achieve the objectives such as its thermal properties and solar absorption.

2.1 Theoretical background

2.1.1 Black Body physics

In physics, the expression ‘black body’ refers to an object that absorbs all radiation incident on it and reflects nothing. A blackbody isn’t really black. It can and does radiate light arising from its thermal energy which can be seen in everyday objects like an electric stove, as its coil heats up it lights up and shifts through a range of colors from a dull red to blue in higher temperatures. In 1900 German physicist Max Planck proposed a mathematical model that describes how a blackbody emits that radiation as a function of the body’s temperature. Now, if the temperature of this blackbody increases, two significant changes occur. Firstly, the total amount of energy that the blackbody emits increases. This is because, according to the Stefan-Boltzmann law, the total energy radiated per unit surface area of a blackbody is directly proportional to the fourth power of its absolute temperature.

Secondly, the frequency of the outgoing radiation also increases. In other words, the wavelength of the radiation decreases. This is a consequence of Wien’s displacement law, which states that the blackbody radiation curve for different temperatures peaks at a wavelength inversely proportional to the temperature.

The visible spectrum of light, which is what we humans can see, ranges from red light (with lower frequencies

and longer wavelengths) to blue light (with higher frequencies and shorter wavelengths). So, when the blackbody gets hotter and the frequency of the emitted radiation increases, the peak of the emission spectrum shifts to shorter wavelengths. This shift implies that the color of the light will move from the red end of the spectrum towards the blue end. Hence, an increase in temperature of the blackbody would cause it to appear to change color from red to blue.

Planck's law

This law describes the spectral density of electromagnetic radiation emitted by a black body in thermal equilibrium at a given temperature (T), as a function of frequency or wavelength. The mathematical form of Planck's law is given by:

$$B(\nu, T) = \frac{2h\nu^3}{c^2} \frac{1}{e^{\frac{h\nu}{kT}} - 1}$$

where:

- ($B(\nu, T)$) is the spectral radiance (the power per unit solid angle and per unit of area normal to the propagation),
- (ν) is the frequency of the radiation,
- (T) is the absolute temperature of the body,
- (h) is Planck's constant
- (c) is the speed of light, and
- (k) is the Boltzmann constant.

This equation implies that the energy of a quantum of light, a photon, is proportional to its frequency, with (h) being the proportionality constant. This was a radical departure from classical physics, which treated light as a continuous wave. Planck's law accurately describes the observed spectral radiance of black bodies and resolves the so-called "ultraviolet catastrophe" predicted by Rayleigh-Jeans law for short wavelengths. The introduction of quantized energy levels was a groundbreaking concept that set the stage for the development of quantum mechanics.

Kirchhoff's law

Kirchhoff's law of thermal radiation states that for an object in thermal equilibrium, the emissivity (its effectiveness in emitting energy as thermal radiation) of the object is equal to its absorptivity (its effectiveness in absorbing energy as thermal radiation).

$$e_f = J(f, T)A_f$$

where e_f is the power emitted per unit area per unit frequency by a particular heated object, A_f is the absorption power and $J(f, T)$ is the universal function that depends only on the light frequency f and the absolute temperature of the body T . Thus a blackbody absorbs all incident radiation, therefore $A_f = 1$

2.2 Carbon Nanotubes (CNTs)

Carbon nanotubes (CNTs) are cylindrical molecules made of single-layer carbon atoms, also known as graphene. They were first discovered by Sumio Iijima in 1991¹⁶, and since then they have attracted a lot of attention from various disciplines, such as physics, chemistry, academia, and industry, due to their remarkable properties arising from their nanoscale structure.¹⁷ Among these properties, nanotubes have exceptional mechanical, electrical, and thermal characteristics. In this work, we focus on the thermal aspect of CNTs and examine it in more depth. Furthermore, we also review the current classification of CNTs based on their main structural features.^{18 19}

- **Shape:** There are Single wall carbon nanotubes (SWCNTs), double walled (DWCNTs) and multi walled carbon nanotubes (MWCNTs), this differentiation is made from the number of layers the CNT has.²⁰
- **Chirality:** The chirality of a carbon nanotube is a property that describes how a graphene sheet is rolled up to form a tube. It is defined by a pair of integers (n,m) that specify the direction and length of the chiral vector, which is the vector that connects two equivalent points on the graphene lattice. The chiral vector is also perpendicular to the axis of the tube and defines its circumference. The chirality of a carbon nanotube affects its electronic and optical properties, such as whether it is metallic or semiconducting, and what is its band gap and absorption spectrum
- **Defects and vacancy:** CNTs have a well-defined ideal structure, but in reality, they often contain some structural imperfections that arise from the synthesis process. These imperfections can be classified into two main types: Stone-Wales defects and vacancy defects. Stone-Wales defects are topological defects that result from the rotation of a carbon-carbon bond by 90 degrees. This changes the hexagonal lattice of the graphene sheet into a configuration of two pentagons and two heptagons. This is called a 5-7-7-5 defect. Another variant of Stone-Wales defect occurs when a carbon atom is removed from a pentagon and new bonds are formed. This is called a 5-8-5 defect. Vacancy defects are point defects that occur when a carbon atom is missing in the graphene sheet and no new bonds are formed. This creates a hole in the lattice.^{21 22 23 24 18}

2.2.1 Double-walled and Multi-walled carbon nanotubes

Both Doublewalled and Multiwalled carbon nanotubes (MWCNTs) are kinds of carbon nanoallotrope composed of more than one wall, ideally based on hexagonal carbon lattice wrapped into cylindrical tubes.²⁰ For Doublewalled CNTs, as the name implies, is formed by two layers of graphene. For MWCNTs this structure goes from 3 to over 20 walls²⁵. MWCNTs are composed of several single-walled nanotubes bonded mainly by van der Waals forces.²⁶ This is fascinating because it enables the individual tubes of MWCNTs to slide or rotate relative to each other, creating nearly perfect linear and rotational nanobearings. The inner shells of MWCNTs can also move telescopically and exhibit remarkable mechanical properties.²⁵ These features allow multi-walled nanotubes to be used in various applications, such as enhancing the mechanical or electrical properties of a material.

There are two models to describe the structure of MWCNTs: the Russian Doll model²⁷, which assumes that graphene sheets are aligned in concentric cylinders, and the Parchment model, which assumes that a single graphene

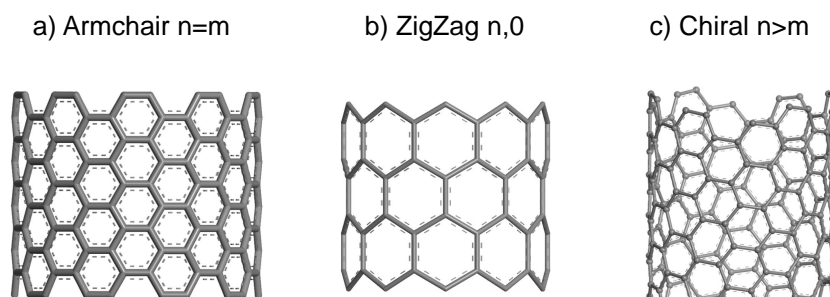


Figure 2.1: CNTs with different chirality based on the indexes n and m . Computer generated images using Materials Studio

sheet is rolled around itself, like a scroll. The Russian Doll model is more prevalent.²⁸ Moreover, the interlayer spacing in MWCNTs is similar to the spacing between graphene layers in graphite.^{24,26,23} MWCNTs can be synthesized in large amounts and are simpler to purify than single-walled or double-walled nanotubes. This lowers their production costs and makes them suitable for diverse scientific fields.^{24,25}

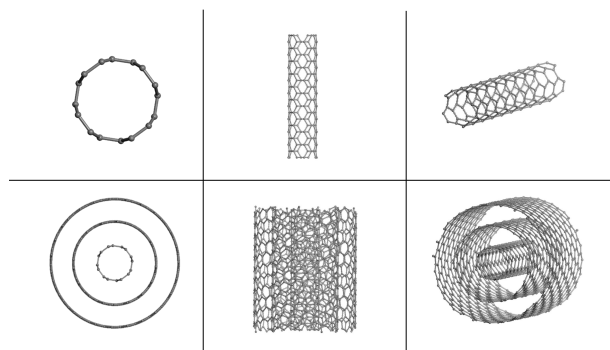


Figure 2.2: SWCNT and MWCNT from different perspectives. Computer generated images using Materials Studio

2.2.2 Thermal properties of CNTs

Black materials are widely used for various applications. For instance, efficient emitter or absorber for energy conversion and shields for stray light and coatings for detectors²⁹. Vertically aligned MWCNTs have reported to

have an absorptance greater than 97% for near infrared wavelengths³⁰. However, scattering by the lack of purity in the sample, defects and misalignment are related to the increase in reflectance and light scattering²⁹. Additionally, it was found that coatings of vertically aligned CNTs improve the emissivity and has a lower dependence on wavelength^{31 32 33}.

Thermal conductivity and transport of thermal energy could be considered to be ruled by phono conduction mechanisms, however the predominantly basis attributed to the collective vibrations of atoms³⁴. The thermal conductivity of CNTs depend on various factors ranging from structure and morphology, size parameters such as length and its functionalization³⁵. CNTs conductivity can range from 2000 to 6000 W/mK depending on the previously stated variables and the measurement methods³⁵. In Figure 2.3 we can observe the relation between thermal conductivity and the defect concentration, which give us insight of possible room for improvement for efficiency^{36 37 38 39 40}.

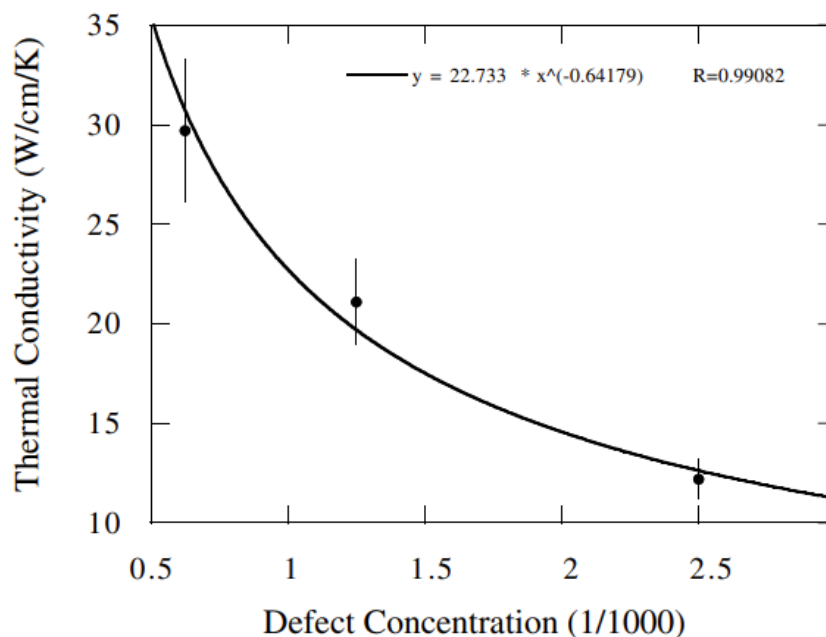


Figure 2.3: Thermal conductivity as a function of defect concentration. Figure from⁴

2.2.3 Thermodynamics and exergy analysis

In order to quantify and understand thermal and chemical processes, exergy was developed with contributions to its principles and practice for over 100 years and with an even faster pace since 1970 with contributions F. Bosnjakovic, J. Keenan and many more scientists and engineers⁴¹, giving as a result the ability to measure sources of inefficiency.

This thermodynamic considerations allow engineering to apply cost-effective improvements of existing systems or even at early stages of design, to quantify and optimize in annualized costs.

Exergy comes into account when two systems of different stages, come into equilibrium and thus in principle work can be developed. One of this two systems can be defined as the environment and the other is the subject of the analysis. Thus exergy is the maximum theoretical work obtainable as the system interact to equilibrium⁴¹. This quantity is very useful in engineering and historically used for coal or hydrocarbon fueled systems, however due to the need for a transition to renewable energy sources (RES), this analysis comes into consideration for RES optimization and comparison to fossil fuel sources⁴².

$$E = U + P_0V - T_0S - \sum_i \mu_{i0}n_i \quad (2.1)$$

From the Euler relation of thermodynamics we can describe the exergy of a system, measured in joules (J). In equation 2.1 Exergy can be defined as the potential work that can be extracted from a system in an initial state A when it is brought to equilibrium with the environmental state A_0 . With U being the total energy of the system, VP_0 being the description of the volume occupied in the system at a pressure P_0 , minus the environment temperature of the system T_0S , being the disordered part of the energy (entropy) in the system U . Lastly the energy of the ambient substances $\mu_{i0}n_i$, the chemical potential for substance i and the number of moles of the substance i .

Later, using Gibbs relation,

$$U = ST - VP + \sum_i \mu_{i0}n_i \quad (2.2)$$

The subsequent formula is obtained from Equation 2.4.

$$E = S(T - T_0) - V(P - P_0) + \sum_i n_i(\mu_i - \mu_{i,0}) \quad (2.3)$$

for this work $P = P_0, \mu_i = \mu_{i,0}$. Thus, the exergy can be an expression of:

$$dE = dS(T - T_0). \quad (2.4)$$

By using the thermodynamic relations $dQ = cdT$ and $dQ = TdS$:

$$E = c \int_T^{T_0} (1 - T_0/T)dT. \quad (2.5)$$

Lastly, for a function of T and T_0 , the exergy of the system is:

$$E = \left| c(T - T_0) \left[1 - \frac{T_0}{T - T_0} \ln\left(\frac{T}{T_0}\right) \right] \right|. \quad (2.6)$$

Giving us an expression for exergy in relation both the temperature of the system and the temperature of the environment, with c being the heat capacity of the medium. Because exergy can reach 0 but no negative energy, the absolute value is placed. This analysis of equation 2.6 is developed in A. Huera bachelors thesis .⁴³

Method	Carbon source	Catalyst	Product
CVD	Acetylene	Titanate modified palygorskite	FeCnanowires
	Methane	Fe-Mo	SWCNTs
	$CaCO_3$	K-doped Co and Co-Fe	MWCNTs
	Different metals	Rare earth promoters	CNTs
	Single crystal of sapphire / quartz	-	Aligned CNTs

Table 2.1: Reported CVD production parameters taking into account catalyst and product. Adapted table from⁸⁹.

2.2.4 Experimental background

Chemical Vapour deposition for CNTs

CVD is a widely used material processing technology in which thin films are formed on a heated substrate with a gas-phase precursor⁴⁴⁹. To produce high-quality thin films using CVD, appropriate equipment is necessary. Custom-made systems offer the operational flexibility often sought by CVD researchers.⁵⁹To maintain and control the result of the deposition, different parameters are needed to be taken into account:

- Gas delivery system
- Reaction chamber
- Vacuum system
- Energy system
- Exhaust gas treatment system

To create the desired synthesis different methods for material growth have been developed:

- Substrate pretreatment^{45 27}
- Heating and annealing
- High-temperature growth
- Cooling

The main techniques for CNTs can be divided into three main processes: Laser ablation, arc discharge and CVD. Among the various synthesis methods, the Chemical Vapor Deposition (CVD) techniques stand out. They are particularly appealing due to their scalability and their aptness for producing nanotubes for sophisticated applications in electronics and optoelectronics. Moreover, they are ideal when there is a need for stringent and customized control over the structure of the deposits.^{5 46 8}

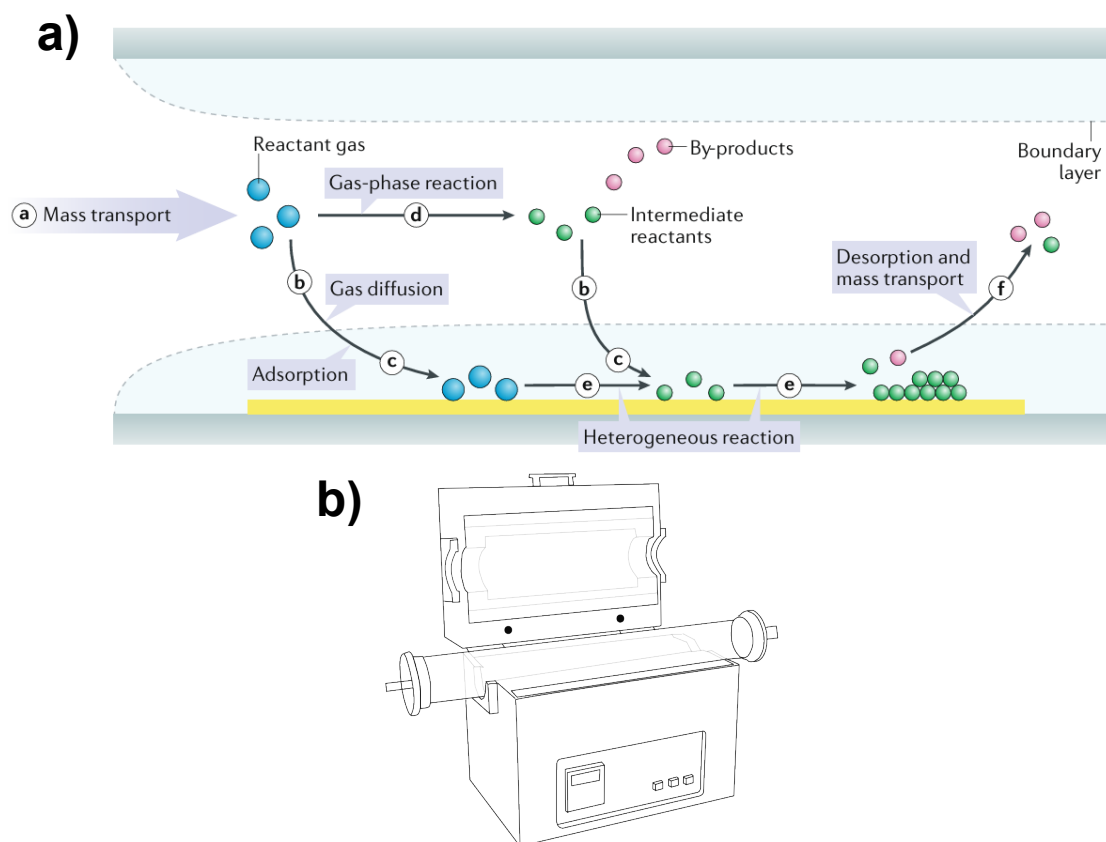


Figure 2.4: (a) CVD reaction process inside the quartz tube. Modified Figure⁵ (b) CVD basic instrument schematic.

2.2.5 Surface pre-treatment for CVD

Surface oxide layers present interfacial resistance by providing a remarkable layer in which electron and phonon transport^{47,44}. Traditionally, to evade the effects of a substrate on the CNT structure, is common for the synthesis process to aim for detached CNTs, as in Si and SiO₂ substrates. The addition of buffer oxide layers is commonly used to enhance the production and quality of CNTs⁴⁸, but also aggravate both electrical and thermal interfacial resistance.⁴⁷ However in order to create a functional substrate, surface modification presents itself not only for a different result of efficiency of the substrate, but also in the structure and defects of CNTs or carbon nanoparticles.⁴⁷ One of the advantages of the modification of the surface is the decrease in synthesis temperature, as low as 650-660 °C for Al substrate, which is below the melting point of the material, giving higher catalytic activity to the surface.^{27,49}

2.3 Characterization techniques

In this study, we employed a trio of analytical methodologies to characterize our samples. These included Raman Spectroscopy, X-ray Photoelectron Spectroscopy (XPS) and Scanning Electron Microscopy (SEM). Detailed descriptions of these techniques will be provided in the following subsection.

X-ray Photoelectron Spectroscopy

X-ray Photoelectron Spectroscopy (XPS), also known as Electron Spectroscopy for Chemical Analysis (ESCA), is a surface-sensitive quantitative spectroscopic technique that measures the energy and number of electrons that escape from the very top layer of material being observed. The fundamental principle of XPS is represented by the equation 2.7 where $h\nu$ is the energy of the incident photon, BE is the binding energy of the electron, and ϕ_s is the work function of the spectrometer.

$$KE = h\nu - BE - \phi_s \quad (2.7)$$

The binding energy, which can be thought of as the energy difference between the initial and final states of an electron, allows us to identify and quantify the elements present on the surface of the material. This is achieved by examining the various energy levels of the final states for each type of atom, as well as the different probabilities or cross sections for each final state relative to the Fermi level.

Through the analysis of the energy and quantity of photoelectrons, XPS can determine the elemental composition of a material's surface. Furthermore, it can provide insights into the depth profile, distribution, and composition of thin films, coatings, or surface contaminants. This makes XPS a valuable tool in a wide range of scientific and engineering disciplines, including materials science, catalysis, nanotechnology, polymer science, and corrosion studies.

Before performing XPS analysis, samples should be cleaned of any volatile or organic material that is not relevant to the study, using methods such as pumping, solvent washing, or cooling. To remove surface layers or native oxides that may interfere with the analysis, surface etching techniques such as ion sputtering or erosion can be applied. Alternatively, fresh surfaces can be exposed by abrasion, fracturing, or scraping the sample, either inside or outside the UHV chamber, depending on the sensitivity of the material to atmospheric contamination. For bulk analysis, samples can be ground to a powder in a mortar and then mounted on various substrates such as adhesive tape, indium foil, metallic mesh, pellets, or dried suspensions.

Raman spectroscopy

Raman scattering occurs when the electric field of the incident light interacts with the molecules or crystals and alters their ability to polarize or respond. The most common type of excitations that cause this effect are the optical phonons. Unlike absorption spectroscopy, where the energy transfer between the light and the material is the main factor, Raman spectroscopy focuses on how the vibrations of the material affect its response to the light.⁵⁰

There are different types of Raman scattering processes, such as first order, second order, resonant, non-resonant, Stokes, anti-Stokes and Breit-Wigner-Fano scattering. These processes depend mainly on the energy and polarization of the incident and scattered photons, the wave vector and frequency of the phonons, and the electronic and vibrational structure of the sample.^{51 52}

The Raman spectra of graphite and SWNTs show many distinct patterns that correspond to different phonon modes and Raman scattering mechanisms. These patterns reveal a lot of information about the unique 1D characteristics of carbon materials, such as their electronic and phonon structures, and the sample imperfections (defects). Moreover, since phonons affect the mechanical, elastic, and thermal properties of the materials, Raman spectra give us a lot of general information about the structure and properties of SWNTs. The classification related to carbon nanostructures will be briefly described below:

- **First-order Raman scattering:** We can have different numbers of phonons emitted before the lattice relaxes, such as one, two, or more, which we name, respectively, one-phonon, two-phonon, and multi-phonon Raman processes. The order of a scattering event is its position in the series of all the scattering events, which may include elastic scattering by a flaw (such as a defect or edge) in the crystal. The simplest process is the first-order Raman scattering process, which produces Raman spectra with one-phonon emission. A scattering event with no change in photon frequency, only in direction, is called Rayleigh scattering of light. For an electron to rejoin with a hole, the difference between the scattered $k + q$ states and k should not be more than twice the photon wave vector. This momentum conservation condition and the small wave vector of the photon explain why we usually see zone-center $q = 0$ or τ point phonon modes in a solid. In SWCNT, the G band spectra is split into many features around 1580 cm^{-1} and the lower frequency radial breathing mode (RBM) are usually the strongest features of SWCNT Raman spectra, both being first order Raman modes. The RBM is a unique phonon mode, is a bond stretching out of plane phonon mode for which all the carbons move coherently in the radial direction and whose frequency is about $100\text{-}500 \text{ cm}^{-1}$, appearing only in carbon nanotubes and the presence of it in a Raman spectra indicates almost certainly the presence of SWCNT.
- **Resonance and non-resonance Raman scattering:** In the presence of an external oscillating field a general resonance phenomenon occurs such as when light is absorbed or emitted between real electronic states, the energy denominators in the oscillator strength become singular. There are two conditions for optical transitions, resonance with an incident or scattered photon. The energy of an incident laser light has the same energy as the energy separation between the two electronic states in resonance, while the scattered photon has an additional energy $\hbar\omega$.

In the case of Single-Walled Carbon Nanotubes (SWCNT), the phonon energies of the G-band are significantly greater than those of the Radial Breathing Mode (RBM) when compared to the resonance energy width. This implies that we can simultaneously observe the RBM and G-band modes under the condition of incident resonance, but not under the condition of scattered resonance.

- **Second-order Raman scattering, D- and G'-band:** Second order Raman scattering involves either two phonon scattering events or a combination of one phonon and one elastic scattering event. In carbon materials,

there are multiple weak Raman signals, the frequencies of which vary with the laser excitation energy. An example is the D-band at 1350 cm^{-1} , which experiences a frequency shift of 53 cm^{-1} when the laser energy is altered by 1 eV. In both graphite and Single-Walled Carbon Nanotubes (SWCNT), the D-band and the G' -band at 1350 cm^{-1} and 2700 cm^{-1} respectively, are examples of one and two phonon second order Raman scattering processes. Meaning D-band spectra can be fitted with two Lorentzians and G' -band can be fitted with one Lorentzian.

- **Stokes or anti-stokes Raman scattering:** This is the process in which an electron scatters by emitting or absorbing a phonon, respectively. The energy of the scattered photon is shifted by the phonon energy from the incident photon. The intensity of the anti-Stokes process depends on the number of thermally excited phonons and the resonance condition for the scattered photon. The ratio of the Stokes and anti-Stokes intensities can be used to determine the temperature and the resonance energy of the nanotubes.

Using experimental and theoretical information M.S. Dresselhaus et. al.¹⁰ provided a summary of the mode frequencies of the pertinent scattering process and the frequency dispersion for all frequencies in the Raman spectra for graphite and SWCNT shown in Table 2.2.

Name	$\omega(\text{cm}^{-1})$	$d\omega/dE_L$	Notes
iTA	288	129	iTA mode, intravalley scattering ($q = 2k$)
LA	453	216	LA mode, intravalley scattering ($q = 2k$)
RBM	248	0	Nanotube only, vibration of radius
D	1350	53	LO or iTO mode, intervalley scattering ($q = 2k$)
LO	1450	0	LO mode, intervalley scattering ($q = 0$)
G	1582	0	Raman active mode of graphite
G'	2700	106	overtone of D mode
2LO	2900	0	overtone of LO mode
2G	3180	0	overtone of G mode

Table 2.2: Properties of the various Raman features in graphite and SWCNTs. Mode frequencies for dispersive modes are given at $E_L = 2.41\text{ eV}$. The term $d\omega/dE_L$ denotes the change of the phonon frequency in cm^{-1} produced by changing the laser energy by 1eV. Modified Table¹⁰.

Scanning electron microscopy

Scanning Electron Microscopy (SEM) is a globally recognized technique for characterizing materials in scientific and technological fields. It's a specific type of electron microscope that can generate images with a resolution of tens of Angstroms, making it suitable for analyzing both organic and inorganic molecules.⁶ The SEM consists of several key components: an electron gun, an anode, magnetic lenses, a sample, and one or more detectors (Figure 2.5 part a). The process begins with the electron gun, which generates electrons either by heating a filament or applying a strong electric field. These electrons are then accelerated towards the anode, which is negatively charged, directing

the electrons towards the sample (Figure 2.5 part b).⁶ The magnetic lenses focus the electrons onto the sample, creating a narrow electron beam. The sample then scatters these incident electrons based on various factors such as its height, chemistry, and crystal structure. The electrons that hit the sample surface are known as primary electrons, and their interaction with the sample can produce a variety of useful results.^{53 54}

Finally, the detector captures the scattered electrons, which travel in different directions and possess different energies. This allows the SEM to provide detailed information about the sample's morphology and composition as seen in Figure 2.5 part c.

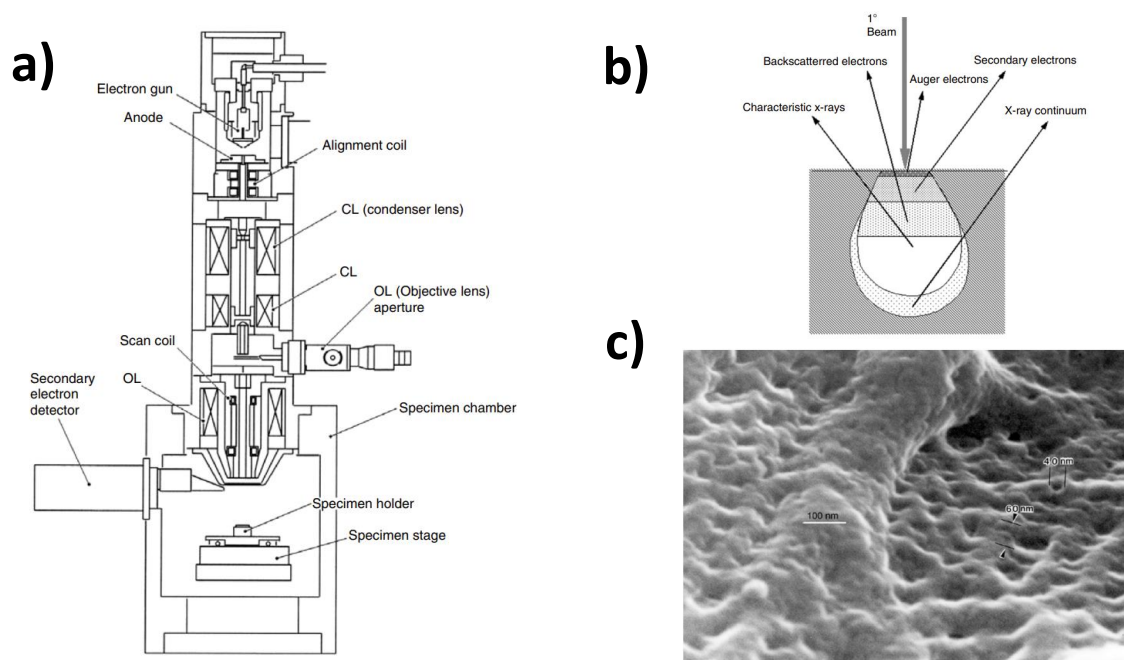


Figure 2.5: a) Schematic diagram of a scanning electron microscope. Modified Figure from⁶ b) Illustration of signals generated by the electron beam-specimen interaction in the scanning electron microscope. c) High magnification SEM (25kV) of luminal surface decorated with 3 nm Au/Pb film

Chapter 3

Methodology

3.1 Surface treatment

3.1.1 Mechanical Methods & Chemical Methods

For the mechanical treatment, both Al and Cu surfaces were polished using a die grinder and its polishing compound until the surface became clear and shiny, this is done with all untreated pieces in order to eliminate any residual element or oxides that might interfere with the structure of the materials deposited over the samples⁴⁸. Later, the substrate goes through a sonication process in order to enhance the texture at micro and nano scale⁴⁷ and enhance the dissolution of elements over the surface. The bath used for this step was a 10% aqueous *NaCl* solution for 10, 20 and 60 min. The effectiveness of this process was visualized using a microscope as pointed in the next chapter.

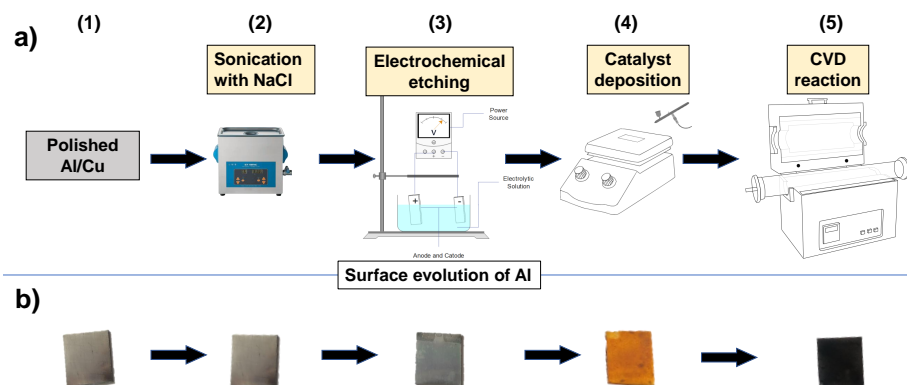


Figure 3.1: Summary of the methodology used in the synthesis of CNTs over metallic plates. (a) Schematic of the treatments used during the synthesis. (b) Evolution of Al samples for each step of the synthesis.

To increase the depth of the texture over the surface, an electrochemical approach was used. Using the parameters described on the Metallographic Handbook from PACE technologies⁵⁵ for each metal such as the electrolyte solution, anode and cathode, lastly the voltage needed in order to achieve the desired texture. This process needed several tries to locate the right voltage and time since the same procedure can be used to polish the surface of the metals.⁵⁶ However the parameters applied where:

- Electrolyte solution: 10% aqueous H_3PO_4
- Current set to 2 A
- Voltage set at 8 V
- For Cu: Cu cathode
- For Al: Stainless steel cathode
- Reaction time 5 min.

Both processes are depicted in Figure 3.3. Part (a) are aluminum samples after sonication in 10% NaCl solution for 60 min. Material from the aluminum is visible as a gray color in the solution. Part (b) are copper samples after sonication in 10% NaCl solution for 60 min. A change in color in the solution indicates the dissolution of material from the surface of the sample and the presence of metal ions which will be deposited on the cathode. Lastly part (c) is copper sample while electrochemical etching in 10% H_2PO_4 as electrolyte and copper as cathode for the reaction of 5 min. The color of the electrolyte solution during the reaction indicate the presence of copper ions.⁵⁶

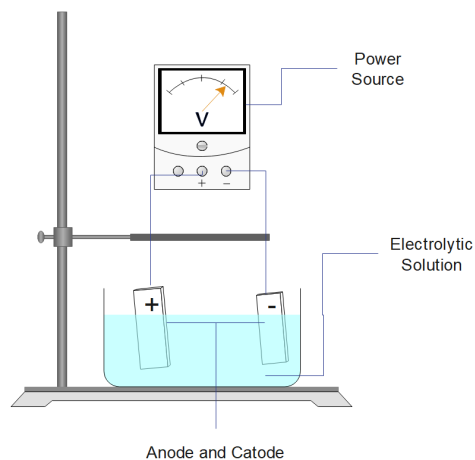


Figure 3.2: Experimental setup schematic for electrochemical etching

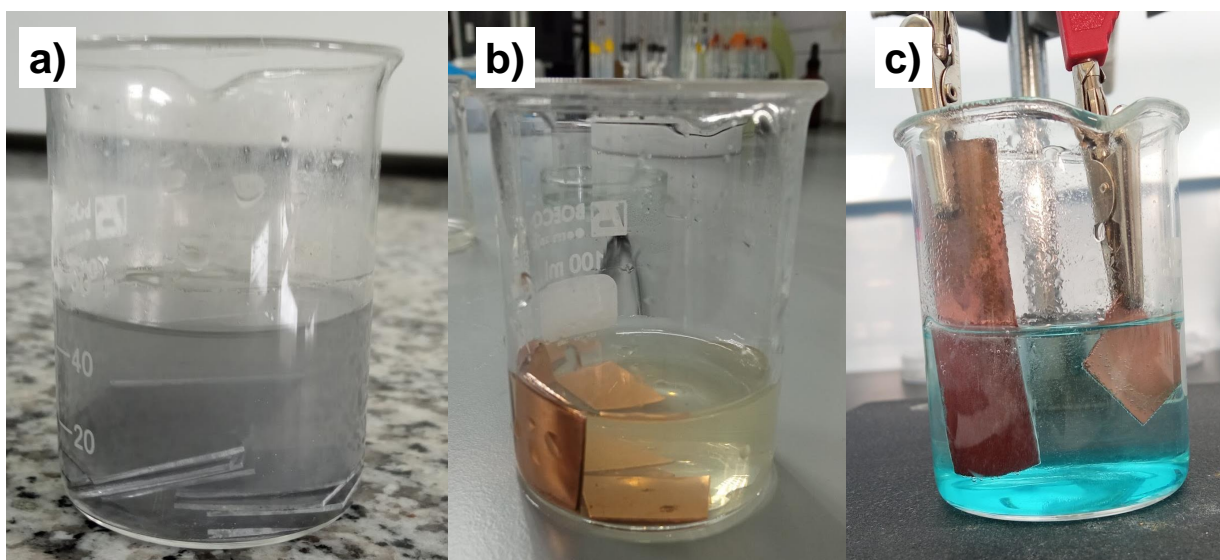


Figure 3.3: Surface treatment of samples. (a) Aluminum after sonication in NaCl solution for 60 min. (b) Copper after sonication in NaCl solution for 60 min. (c) Copper sample during electrochemical etching.

3.1.2 Cathalyst deposition

For the catalyst deposition several methods where tested. The goal was to create a thin film of a solution that enhances the probability and efficiency of CNTs growth over the surface using a solution of Cobalt nitrate and Iron(III) nitrate. Three procedures where tested starting with immersion of the material and sonication of the samples, secondly we used spin coater to create a thin film of catalyst and lastly we used an airbrush over a heated sample. In order to reach a homogeneous spread, several parameters where tried for each technique like different solvents, concentrations and the use of PVC as agglutinant for an even dispersion. However in results we will only cover the ones that resulted in the growth of CNTs over the surface in order to characterize them.

For the sonication process the samples where immersed in the catalyst solution on a beaker and put on an ultrasonic bath for 10, 30 and 60 min using a different beaker for aluminum and copper but the same catalyst solution. The goal of this process was to reach the crevices of the metallic surface for a more even coating and for time efficiency. In order to use the spin coater the viscosity of the catalyst needed to be modified to reach a thin film. An aqueous solution of 10% PVC was used to increase the viscosity since we tried to avoid adding elements or compounds that could affect the synthesis reaction later on. Different parameters like acceleration, speed and time where used for copper and aluminum.

Lastly, airbrush deposition was tested over the samples with and without the heating of a hot plate. The aqueous solution of the catalyst was loaded to an airbrush and from a vertical distance of 10 cm from the sample four coating of the catalyst where given. Later, using a hot plate set to 60-70 °C the samples where heated and given the same treatment .

Substrate	Temperature [°C]	Reaction time [min]	Inert gas	Carbon source
Aluminum	750	15	Ar (450[ml/min])	C_2H_2 (50[ml/min])
		20		
Copper	520	15		
		20		

Table 3.1: Synthesis parameters used for CVD reaction in order to grow CNTs over Al and Cu surfaces.

3.1.3 Synthesis of CNTs using CVD

For this investigation, the carbon nanotubes were synthesized using Chemical Vapor Deposition due to its possibilities for large scale production of CNTs in relatively controllable parameters like temperature, pressure and quartz tube diameter. The parameters used for the synthesis time, carbon source, time and temperature are specified on Table 3.1.

After both surface treatment and catalyst deposition where done on aluminum and copper samples, the Al and Cu surfaces where loaded in a quartz tube with 450 ml/min Argon flow. Using the three temperature zones of the CVD , the first and second ones were set to 750 °C and that's where the copper samples where placed. The third zone averaged 520 °C and the Aluminium samples where placed there due to its melting point. All samples where heated until the desired temperature was reached and kept for 15 min under an acetylene C_2H_2 50 ml/min flow for the synthesis reaction to take place.⁵⁷ Lastly the samples where cooled under 450 ml/min Ar flow. This process was not used for Cu and Al samples with uneven catalyst deposition.^{43 58 59}

3.1.4 CNTs characterization

To identify the type and morphology of the grown CNTs as well as the characteristics of the etched metallic surfaces, we used spectroscopic and microscopy methods. For Raman spectroscopy where acquired using Horiba LabRAM AM HR Evolution, using 532 nm laser excitation. The surface chemical analysis where carried out using PHI VersaProbe III X-ray Photoelectron Spectrometer (XPS). The Scanning Electron Microscopy was performed using MIRA3 TESCAN, instrument owned by Universidad de las Fuerzas Armadas ESPE- CENCINAT.

3.1.5 Measuring heat capture of CNT-grown metallic surfaces

The measurement of the heat capture of the treated samples is designed in such way that the hypothesis of this work is tested. The efficiency of solar heat capture is tested on both CNT-Al and CNT-Cu to compare the capacity of the material to harvest radiation and transform it into heat as well as the difference with the surface activation treatment with no reaction synthesis. The materials tested where are listed below:

1. **Carbon nanotube/etched Copper (CNT-Al):** A 2x2 cm copper sheet subjected to mechanical etching using a sonic bath on 10 wt % NaCl solution for 2 hours and chemical etching using H_2PO_4 as an electrolyte and copper as cathode. Later treated using CVD at 750°C for 15 min using acetylene as carbon source.

2. **Carbon nanotube/etched Aluminium(CNT-Cu):** A 2x2 cm aluminium sheet subjected to mechanical etching using a sonic bath on 10 wt % NaCl solution for 2 hours chemical etching using H_2PO_4 as an electrolyte and stainless steel as cathode. Later treated using CVD at 520 °C for 15 min using acetylene as carbon source.
3. **Etched Copper:** A 2x2 cm copper sheet subjected to mechanical etching using a sonic bath on 10 wt % NaCl solution for 2 hours and etched using H_2PO_4 as an electrolyte and copper as cathode.
4. **Etched Aluminium:** A 2x2 cm aluminium sheet subjected to mechanical etching using a sonic bath on 10 wt % NaCl solution for 2 hours and etched using H_2PO_4 as an electrolyte and copper as cathode.

3.1.6 Temperature measuring setup

In order to analyse the heat capture of the samples, a device needed to be created so that the measurement could be recorded simultaneously. This was achieved using four PT100 temperature sensors connected to an Allen Bradley 1769-ECR PLC programmed to read the temperature of the four sensors simultaneously 5 times per second and print an average of the values for each sensor with the date and time it was captured.

The sensors were attached to a laser cut transparent acrylic structure that holds 4 samples at the same height in regular spaces along its surface. The tips of the pt100 sensors were attached using bolts to the bottom of the space for the samples and covered with computer thermal paste to increase the heat conductivity from the metal to the sensor as in Figure 3.8

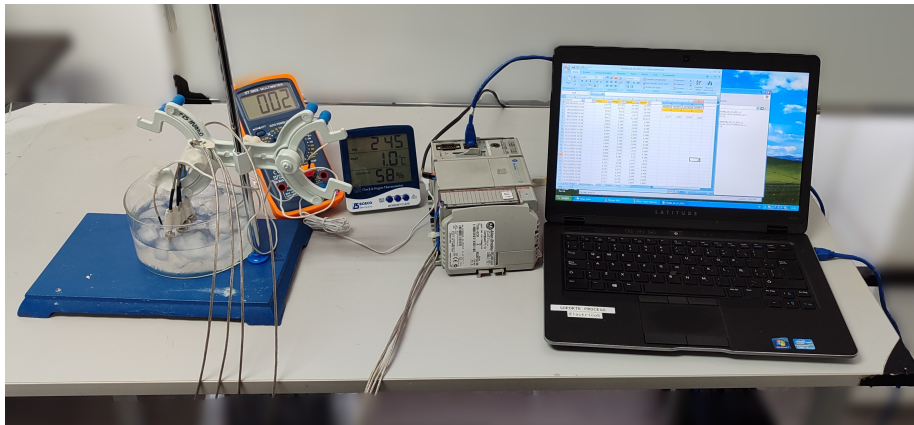


Figure 3.4: Calibration setup. Four sensors submerged on ice water with two reference instruments in order to calculate the offset in each sensor.

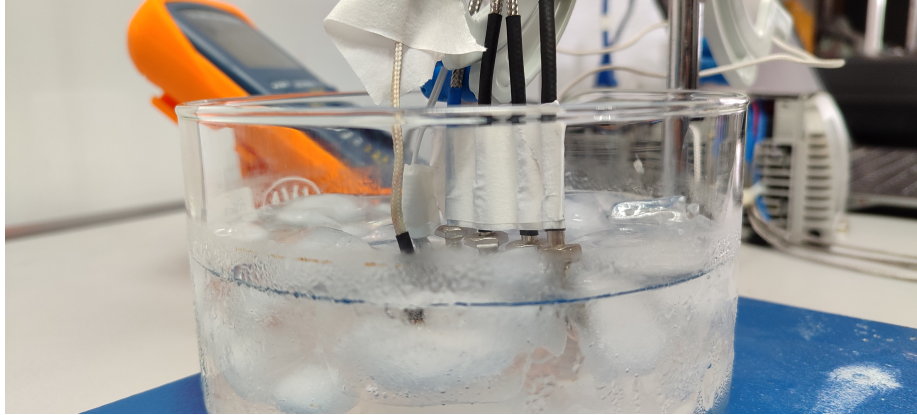


Figure 3.5: Sensor calibration setup. Four sensors and two reference instrument submerged on ice water.

The sensors were calibrated using a linear function with the specific slope value provided by the sensor manufacturer, as well as a temperature reference of freezing water using the setup shown in Figure 3.4. We used two instruments to have a reference as shown in Figure 3.6, the first one being a Boeco Digital Thermo-Hygrometer & Clock with a temperature measurement range of -10 to +50 °C and an accuracy of $\pm 1^\circ\text{C}$. The second reference instrument was a DT-5808 Digital Multimeter with a range of -40 to 1000 °C and an accuracy of $\pm 1^\circ\text{C}$. The readings were a reference to either increase or decrease an offset for each sensor as until it reaches an error margin lower than 0.1 °C as shown in Figure 3.5.

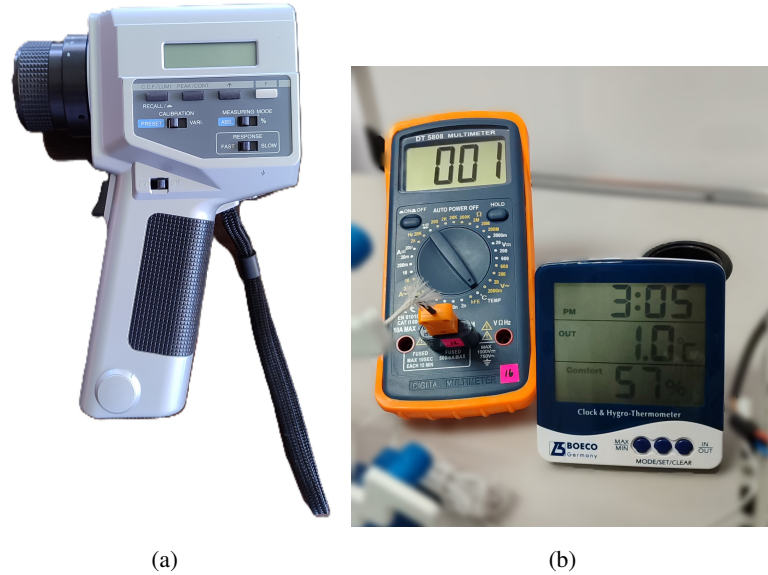


Figure 3.6: (a) Minolta Xs-100A luminance and color meter. (b) Left: DT-5808 Digital Multimeter and right: Boeco Digital Thermo-Hygrometer & Clock. Two reference instruments for calibration of the sensors.

3.1.7 Solar Simulation Chamber (Xenon lamp)

To create a controlled measurement of the material heat capture a Solar chamber was used. This instrument is used to generate controlled sun-like radiation to test photovoltaics and set controlled chemical reactions. The objective of this test is to set a standard to measure the heat capture of the different samples under the same conditions and without extra parameters like humidity, clouds or wind. Once turned on, the xenon lamp needed time to heat up and stabilize its output, reaching 427 W. The samples were fixed to a height of 8 cm under the light of the chamber as illustrated on Figure 3.8.



Figure 3.7: Solar chamber heat capture test of the samples and luminometer setup.

Additionally the luminance of each sample was measured using a Minolta CS-100A Luminance and color meter shown in Figure 3.6 which can measure in candela per meter square cd/m^2 the luminous intensity per unit area of light traveling in a given direction. In this particular case, it describes the amount of light reflected from the sample to a given angle. The setup used was built at an approximated angle of 60° as indicated in Figure 3.7 the measurements were taken every 30 min while being subjected to the lamp .

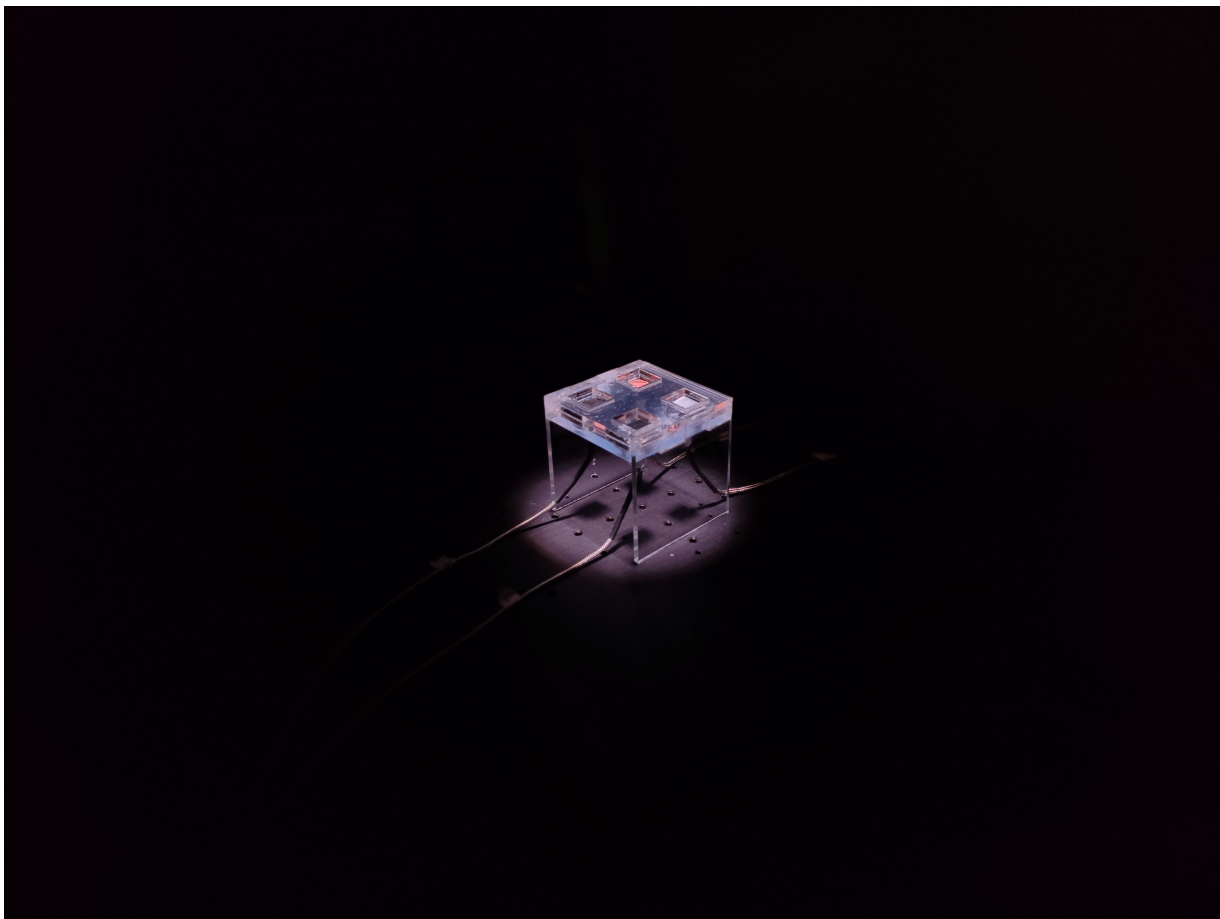


Figure 3.8: CNT-Al, CNT-Cu, etched aluminium and etched copper under the light of the Xenon lamp to measure heat capture.

Chapter 4

Results & Discussion

4.1 Mechanical and Chemical surface treatment

The analysis of the results provided by the surface treatment are shown on Figure 4.1. Over different figures and four stages of visualization we are able to show the effect of etching over both copper and aluminum. The results are detailed in the next subsections.

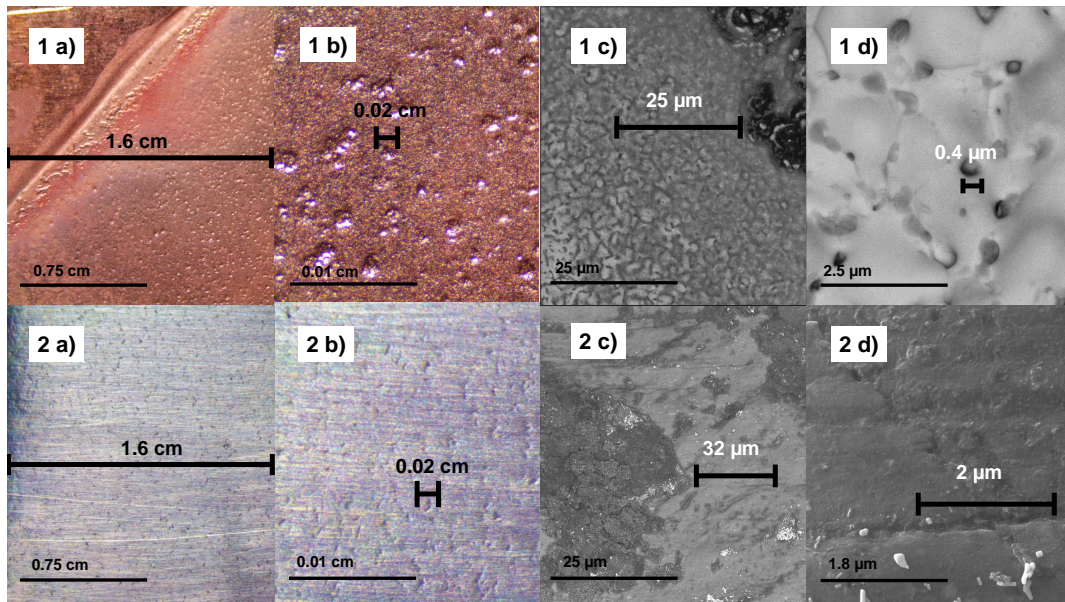


Figure 4.1: Copper and aluminum surfaces after surface treatment. Images obtained with optical microscopy and SEM. Description on Table 4.1

	Microscopy 10x	Microscopy 50x	SEM 6,67 kx	SEM 100 kx
Copper (1)	(1a) Sample after sonication and electrochemical etching. Evenly distributed holes.	(1b) Textured samples. Holes of 0,02 cm in diameter	(1c) Textured sample, visible regular clusters.	(1d) Textured sample with holes of 0,4 μm in diameter.
Aluminium (2)	(2a) Sample after sonication and electrochemical etching. Evenly distributed holes.	(2b) Textured samples. Holes of 0,01 cm in diameter	(2c) Textured sample with topological defects over the surface.	(2d) Textured sample with no evident holes nor specific structure.

Table 4.1: Description of the results shown in Figure 4.1 for each sample

4.1.1 Surface activation/etching

Using the methodology stated in Section 3 two techniques were used: sonication with NaCl aqueous solution and electrochemical etching. The aim was to remove parts of the oxide layer of the materials leaving behind nanostructures on the surface morphology that allow a wider surface area in which the carbon nanostructures can grow^{56,60}. The following paragraphs present the results of each of these techniques.

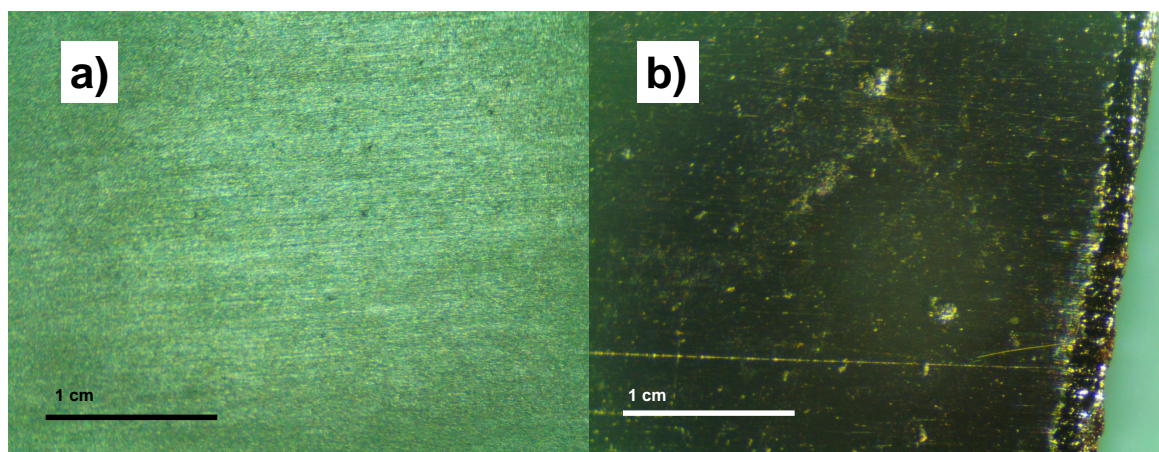


Figure 4.2: Pristine metallic plates under 25x optical microscopy. (a) Aluminum. (b) Copper.

Sonication with NaCl aqueous solution

By using procedures from previous work done with this methodology^{43,47}, a 10% wt NaCl solution was used to breakdown the oxide layer of both copper and aluminum. For aluminum results in part a and c of Figure 4.3 show

that for 30 and 60 min correspondingly the sonication proves to be ineffective and irregular over the surface, however the generation of dots and scratches shows that an increase in time generates scattered abrasions over the surface as depicted in Figure 4.3. In part b chemical etching was tested using 10% wt H_2PO_4 with a voltage of 8 V, 2 A of current for 5 min and dots with mean diameter 0.005 cm appear scattered over the surface. Part c is a combination of both sonication in 10% NaCl and chemical etching controlled with a fresh 10% wt H_2PO_4 electrolyte and the same voltage and current parameters as part c, however the surface shows an even distribution of dots with the same mean diameter of 0.005 cm.

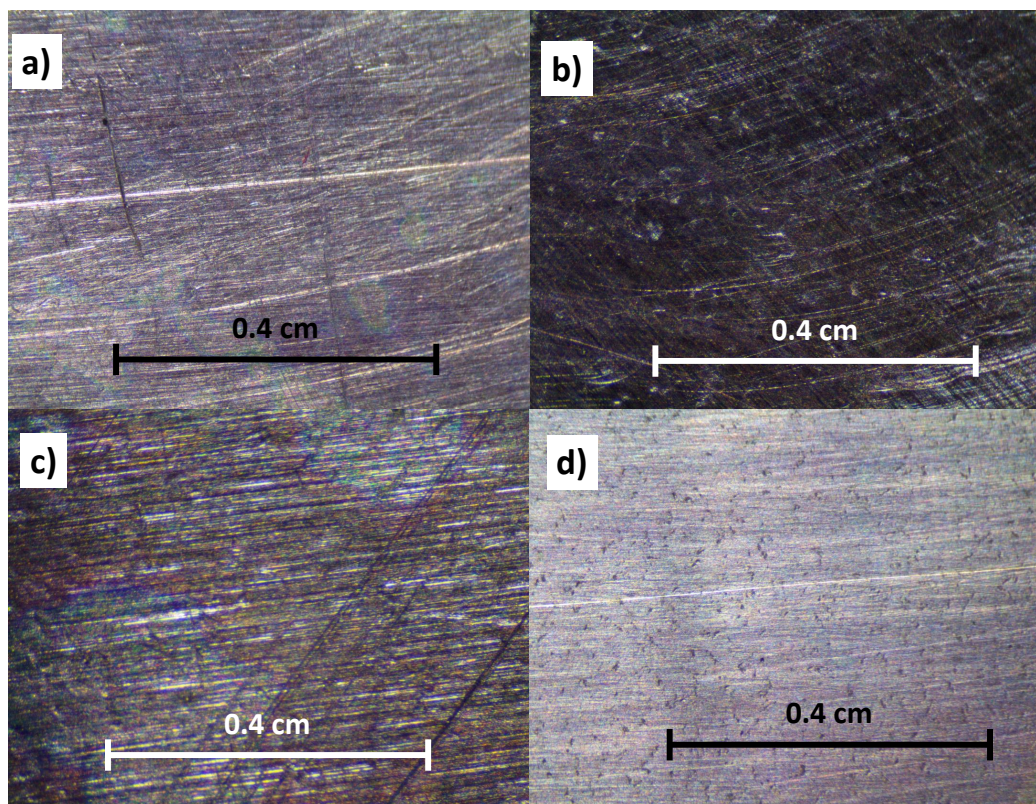


Figure 4.3: Aluminum surfaces after sonication and chemical etching. Image done with optical microscope 50x. (a) Surface after sonication in NaCl for 30 min. (b) Surface after chemical etching. (c) Surface after sonication in NaCl for 60 min. (d) Surface after sonication in NaCl for 60 min and chemical etching.

For copper the same treatment was applied. First sonication with 10% wt NaCl solution and later chemical etching using 10% wt H_2PO_4 as electrolyte. In Figure 4.4 part a and c we can see the results of 30 and 60 min respectively. Part a shows almost no evidence of a morphological modification in comparison to part c, which shows crevices and elevations over the surface with dots scattered as well as change in color for both samples. Part b shows a sample under chemical etching using the same 10% wt H_2PO_4 with a voltage of 8 V and 2 A of current for 5

min as the aluminum sample. The result shows a modified surface structure filled with dots and irregularities with differences of height and depth over the sample. Part d show an even distribution of dots and no dramatic changes in height over the sample, the holes have a mean diameter of 0.02 cm.

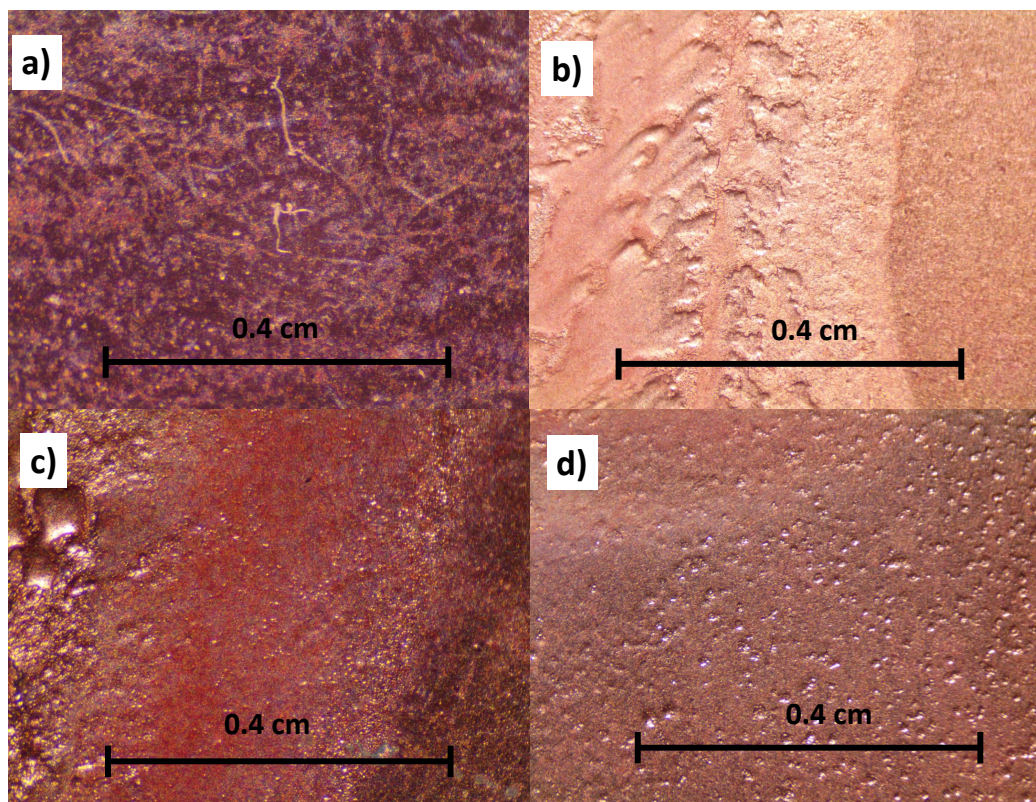


Figure 4.4: Copper surfaces after chemical etching. Image done with optical microscope 50x. (a) Sample after 30 min of sonication in NaCl. (b) Sample after chemical etching. (c) Sample after 60 min of sonication. (d) Sample after sonication in NaCl for 60 min and chemical etching.

In Figure 4.5 we can see SEM images from samples under the combined etching methods. At this scale the even distribution of topological defects isn't evident however is clear how the treatment increased the surface area of the sample showing holes and crevices smaller than $1\mu\text{m}$ scattered over the sample. For copper, we can see in Figure 4.6 an almost fractal topological defects show all over the sample, meaning a great increase in surface area. The defects are approximately $0.4\mu\text{m}$ in diameter and hollow.^{56 60}

In conclusion, a combination of both sonication with NaCl and chemical etching proves to be effective for the modification of aluminum and copper surfaces in comparison to pristine samples Figure 4.2, showing microscopic defects all over the samples. However, copper in comparison proves to give better results for the objective of surface area increment. Fractal structures and nanopiramidal structures⁶¹ provide space for nanometric structures to deposit

over the surface.^{56 60 45}. This results were obtained using image analysis from optical microscopy as well as SEM results using ImageJ software to set the correct scale.

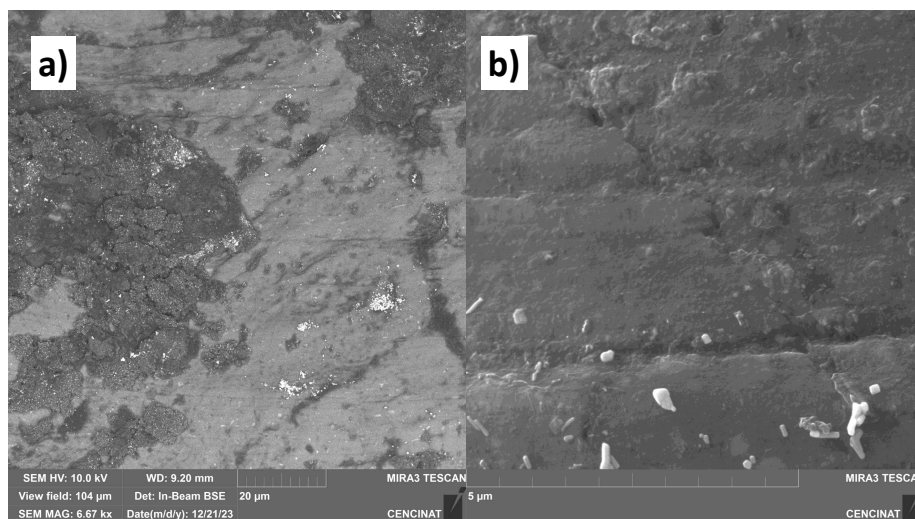


Figure 4.5: SEM of aluminum samples after sonication with 10% wt NaCl for 60 min and electrochemical etching using 10% wt H_2PO_4 as electrolyte with 8 V, 2A for 5 min . a) SEM MAG: 6.67 kx. b) SEM MAG: 100 kx.

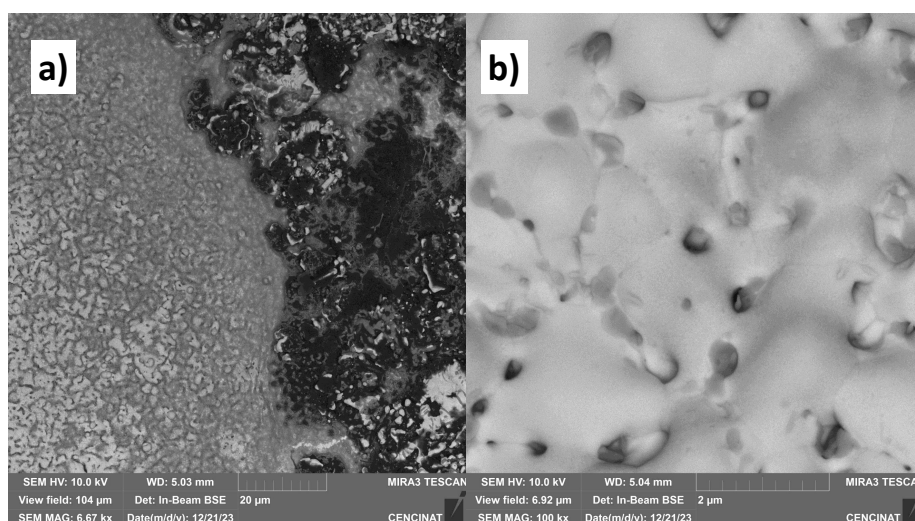


Figure 4.6: SEM of copper samples after sonication with 10% wt NaCl for 60 min and electrochemical etching using 10% wt H_2PO_4 as electrolyte with 8 V, 2A for 5 min . a) SEM MAG: 6.67 kx. b) SEM MAG: 100 kx

4.2 CNT growth over copper and aluminum using CVD.

To produce CNT over copper and aluminum on the same reaction, a different temperature gradient was needed. Using the parameters stated in Chapter 3 for CVD reaction we obtained favorable results for both copper and aluminum. The copper reaction was carried out at 750 °C and for aluminum the substrate temperature reached 520 °C^{61,5}. The evolution of the samples can be seen in Figure 4.7. Going from a polished state, then surface treatment, catalyst deposition and lastly the result after the reaction. Based on the literature we used a reaction time of 15 min for the

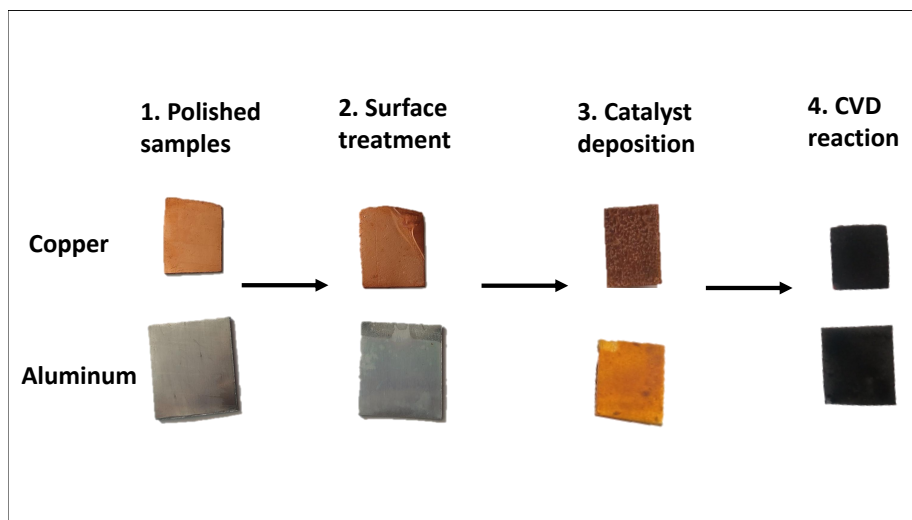


Figure 4.7: Evolution of the metallic samples after 1) Polishing 2) Surface treatment 3) Catalyst deposition and 4) CVD synthesis.

first reaction and 20 min for the second^{46,33,5}. In part 4 of the Figure 4.7 we can see an even black coating over the metallic sample. This coating had a mean height of 0.7 mm for 15 min reaction, over different test and its consistency was fragile to movement, the outermost pieces of material seem to crumble when shaken. In both cases the coating presented a deep black appearance, however for the copper samples it had a slight brown color over the surface. For the 20 min reaction we observe a black coating of with a mean height of 1.1 mm and fibers of material growing out of the edges of the sample. The consistency was less brittle, however the colour of both CNT-Al and CNT-Cu had a brown aspect. This samples were less evenly coated with nanotubes and surface elements (in the case of aluminum) were pushed off from the sample. See Figure 4.8. In further sections the quality of the samples was characterized using Raman spectroscopy.

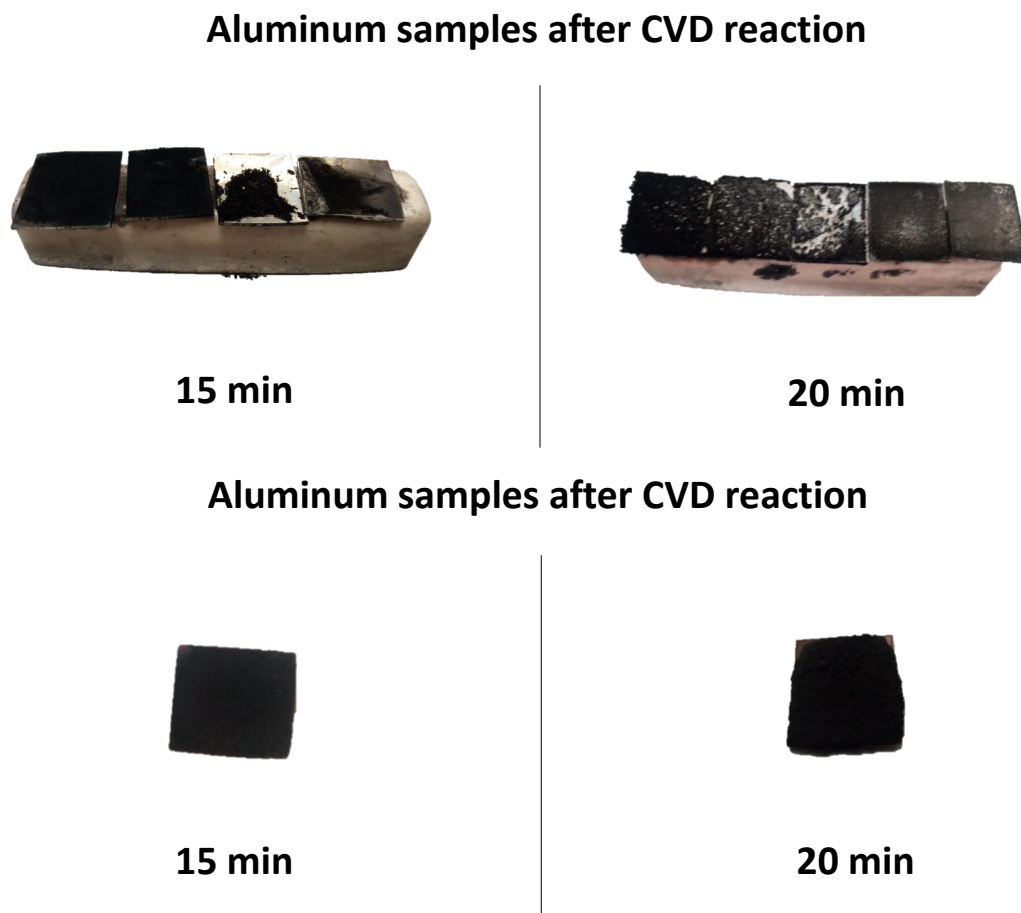


Figure 4.8: CNT -Al and CNT-Cu samples after 15 and 20 min of reaction time in CVD.

4.3 Scanning Electron Microscopy (SEM) characterization of CNTs

To better determine and analyse the results of the synthesis we used SEM in order to visualize the structure of the samples. Due to the increase of the surface area produced by the surface treatment and the height of the carbon structures SEM captured different structure with a single sample. For CNT-Al seen in Figure 4.9 we can differentiate nanotubes of different sizes. In part a fibers of 30 nm and in part b tubes of 110 nm in diameter are scattered in the sample proving the existence of CNTs. This tubes show particles with the same diameter of the tube at the top of the structure, meaning it had a bottom up formation around the particle⁴⁹.

However for CNT-Cu similar shown in Figure 4.10 structures are not shown and fibers of 67.5 nm in diameter can be seen in part a, for part b we have almost spherical particles which can be encapsulated particles or C-C structures, meaning that the tubular structure of long CNTs is not present. In both samples the CNTs grown are

not aligned which could affect the thermal capacity and the heat capture of the samples.⁶² Based on SEM images 4.9 4.10, elucidates the range in which multiwalled nanotubes diameters vary and their bundled forms. We observed individual nanotubes spanning from 30 to 110 nm and bundled structures up to 1 μm . The wide variety of structures among these findings underscore the structural diversity critical for many nanotechnology applications.

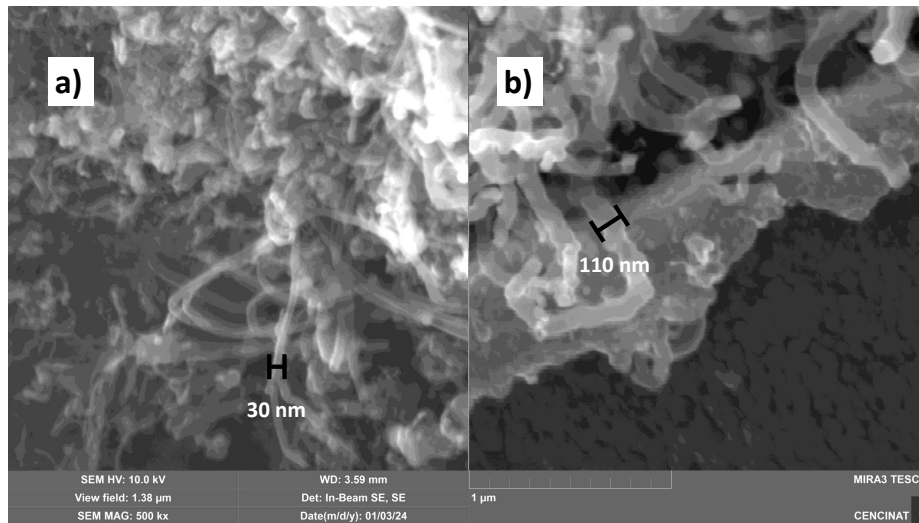


Figure 4.9: SEM images of CNT-Al with a) SEM MAG: 500kx b) SEM MAG: 300kx

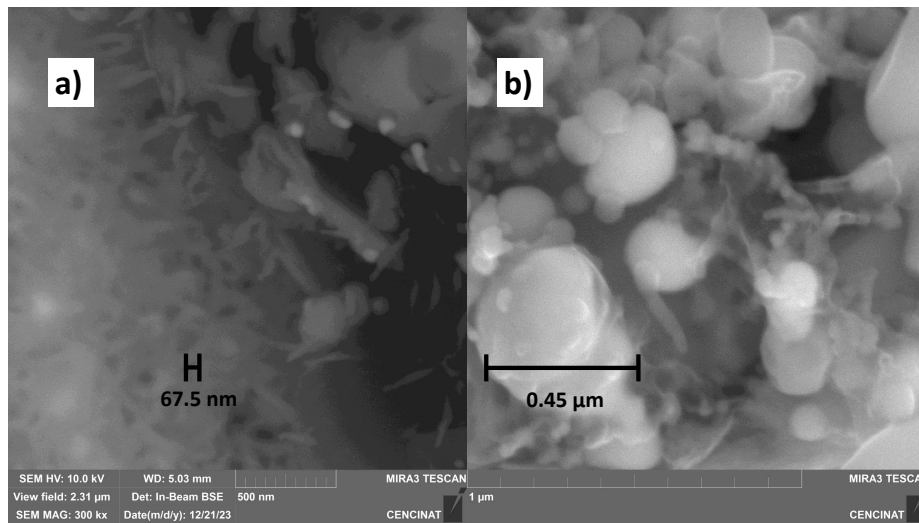


Figure 4.10: SEM images of CNT-Cu with a) SEM MAG: 300kx b) SEM MAG: 500kx

4.4 Raman Spectroscopy of CNT-Al/-Cu

The analysis of carbon nanostructures was heavily dependant on Raman spectroscopy due to the widely reported characteristics of CNTs^{10,24,63}. The information gathered by this technique allow us to identify the structures synthesized, the quality and the shape. The results of the spectra from the CNTs are shown in Figure 4.11 and Figure 4.12 for different readings of the parameters used for each reaction. The spectra were taken using a 532 nm laser as excitation wavelength.

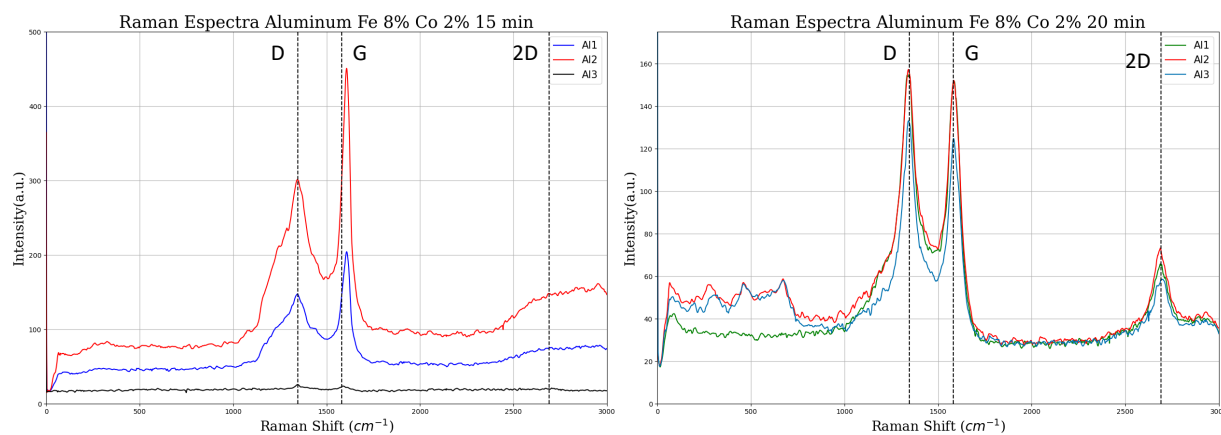


Figure 4.11: Raman spectra of three zones (Al1, Al2, Al3) of CNT grown over aluminum using Fe-Co catalyst with a reaction time of 15 min (Left) and 20 min (Right). Laser 532 nm.

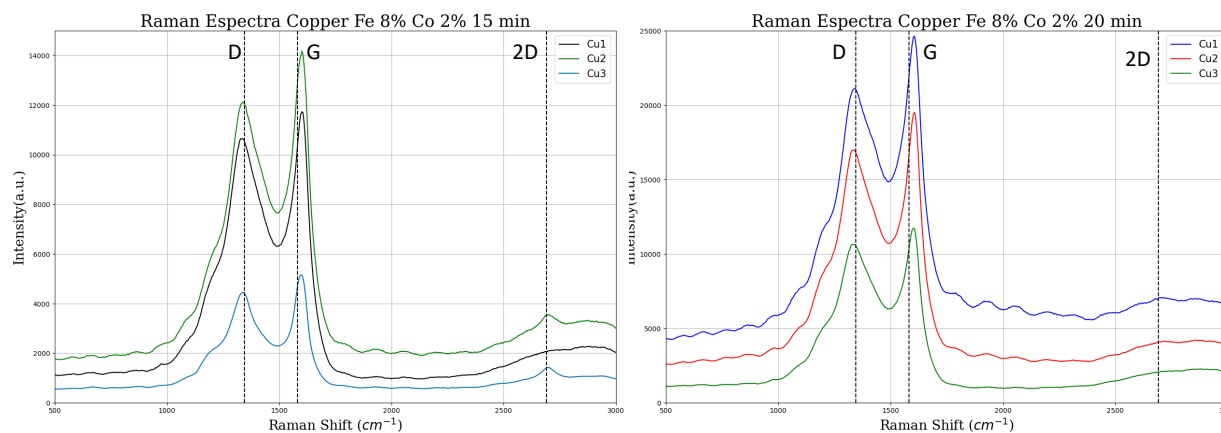


Figure 4.12: Raman spectra of three zones (Cu1, Cu2, Cu3) of CNT grown over copper using Fe-Co catalyst with a reaction time of 15 min (Left) and 20 min (Right) Laser 532 nm.

From Figure 4.11 and Figure 4.12 we can observe different spectra within a single sample, meaning the reaction would not only give us one type of carbon structure, but a bulk of different structures and hybridization. According to¹⁰ and using table 2.2 we can determine the typical features of MWCNTs structure D,G and 2D bands, with the center of the curve around 1346, 1582 and 2692 cm^{-1} respectively.

Conversely, as stated in^{10,24}, the D and G band peaks for a reference MWCNTs material of 100% purity are positioned at 1350 and 1582 cm^{-1} respectively. The position of the G-band peak from this study aligns with the reference MWCNTs material, while the D-band peak's position varies. This variation could be due to the fact that, as stated in source¹⁰ the position and intensity of the D-band peak fluctuate significantly with the laser's excitation wavelength.⁶⁴ The curve fitting shown in Figures 4.13 and 4.14 were done with python , locating the Lorentzian

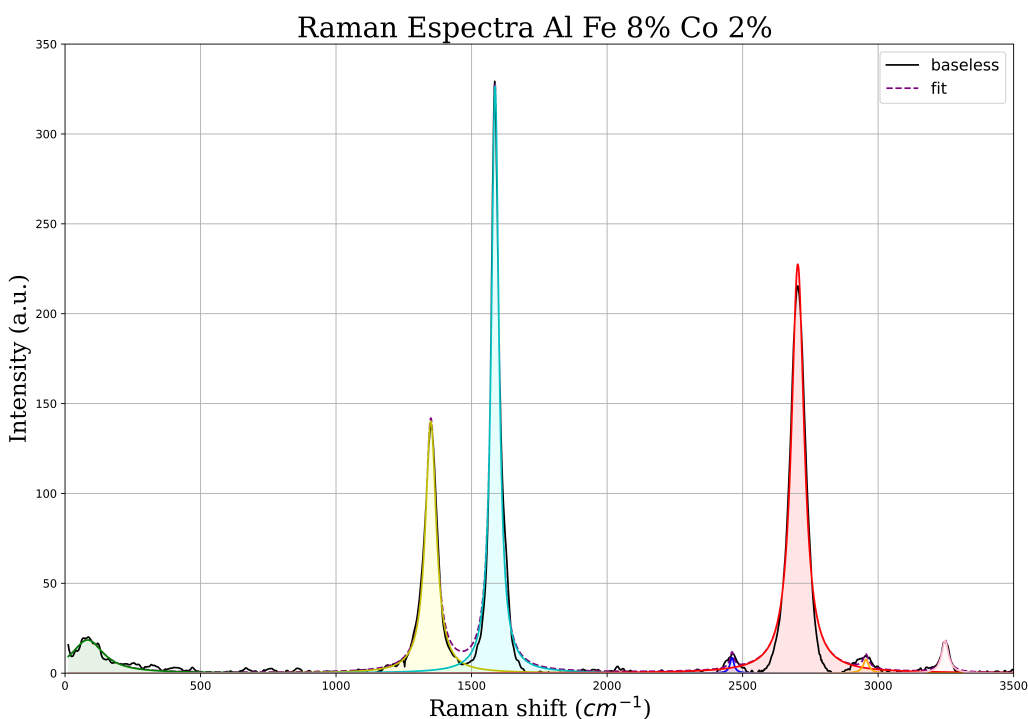


Figure 4.13: Lorentzian curve fitting for CNT-Al sample. Calculations and baseline removal made in Python.

curves after removing a baseline specified in APENDIX 1. This process allowed to spot different bands and peaks from the resulting reading. The Lorenzian associated to the D band has its center located in 1349 cm^{-1} for CNT-Al while for CNT-Cu is a combination between 1417 and 1337 cm^{-1} which according to²⁴ may be related to the LO mode in addition to the D band. For both sample the G band is well defined at 1586 cm^{-1} for CNT-Al and 1604 cm^{-1} for CNT-Cu.

However for 2D band the values are slightly shifted with 2786 cm^{-1} an almost non existent for CNT-Cu at 2931 cm^{-1} which can be attributed to the 2LO mode which is an overtone of the LO mode. In neither CNT-AL or CNT-Cu a RBM mode appears, meaning that MWCNT where grown over the samples.^{63 24}

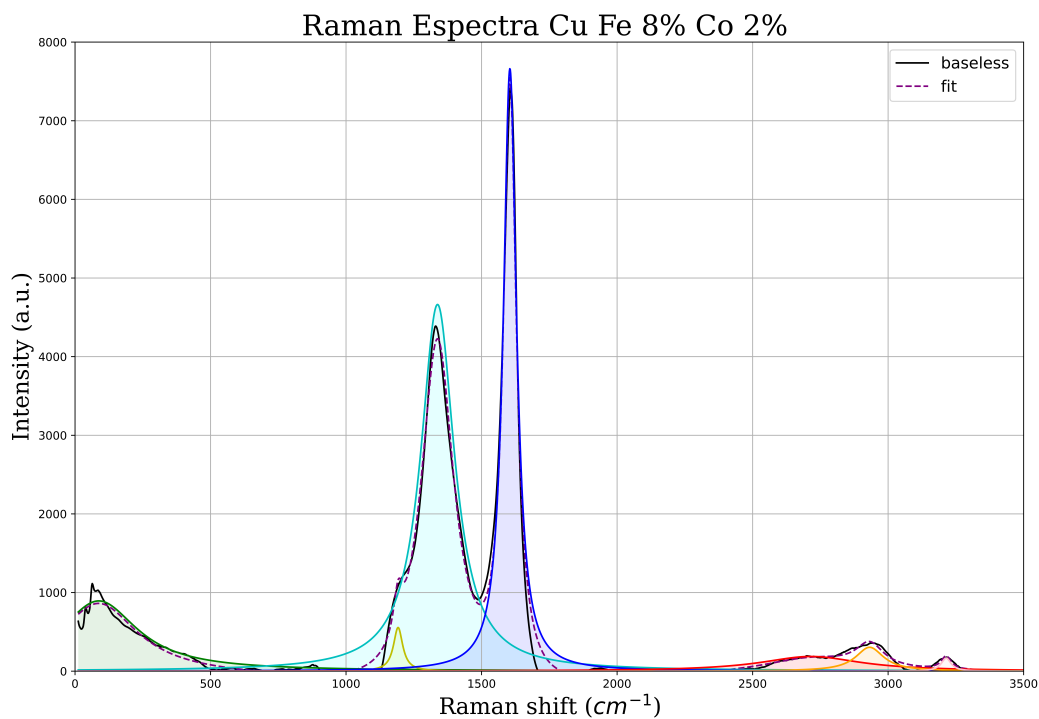


Figure 4.14: Lorentzian curve fitting for CNT-Cu sample. Calculations and baseline removal made in Python.

4.5 XPS analysis of the samples

The chemical composition of the surface after synthesis process is a key step for in order to determine the material used for later tests. Both CNT-AL and CNT-Cu samples where loaded in the XPS (Figure 4.15) and the analysis was performed over a spot with a diameter of $100\text{ }\mu\text{m}$ and 7 nm deep.

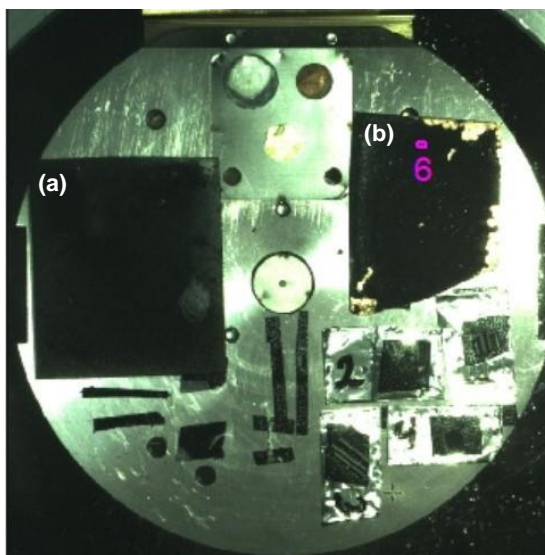


Figure 4.15: CNT-Al and CNT-Cu samples loaded into XPS sample holder

The spectra (a) and (b) in Figure 4.16 have the most intensive peak is located around 285 eV and it is related to C1s. This indicates the presence of different states of carbon in the sample, due to the synthesis and the handling of the samples. Other common peak is around 532 eV for both samples and is related to O1s. For (a) the spectrum shows peaks indicating contamination of Zn over the surface, this is elucidated with peaks around 12, 90, 141, 1023 and 1046 eV corresponding to Zn3d, Zn3p3, Zn3s, Zn2p3 and Zn2p1.

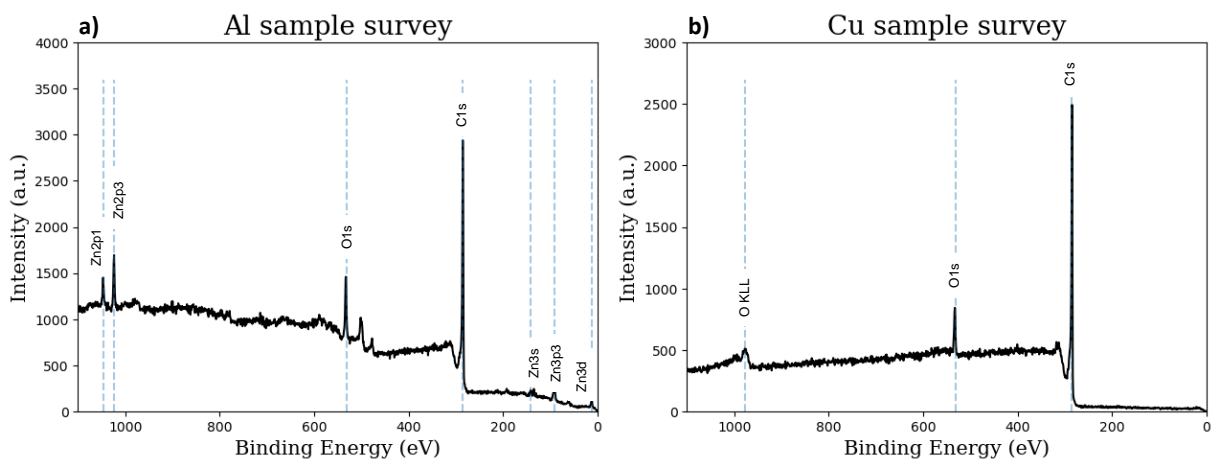


Figure 4.16: XPS survey spectra of (a)Al and (b)Cu samples after surface treatment (surface activation) and CVD reaction.

This type of contamination can be attributed to handling of the samples. Lastly the last peak in (b) is around 977 eV attributed to OKLL, related to the Auger transition involving Oxygen from K (the initial core-level ionization) to L (outer-shell electron).^{65 66}

Using high resolution XPS. In Figure 4.17 show the composition of the peak around 285 for (a) CNT-Al and (b) CNT-Cu. Peaks at 284.7 eV (C-C) represent the sp² and peaks around 285.6 eV (C=C) represent sp³ hybridization of carbon. This gives us information about the structure of MWCNTs.¹⁷ Other peaks are related to the formation of other amorphous carbon structures. In Figure 4.18 the spectrum elucidates the deconvolution of O1s in the sample using high resolution XPS. The results showed peaks around the same binding energy for (a) and (b). This result indicates the presence of oxygen during the synthesis of the material due to ambient exposure, the peaks are around 533, 532, 534 eV related to C-O, C=O and organic C-O correspondingly.⁶⁶ Voigt function was used to deconvolute the specific peaks of C1s and O1s samples.

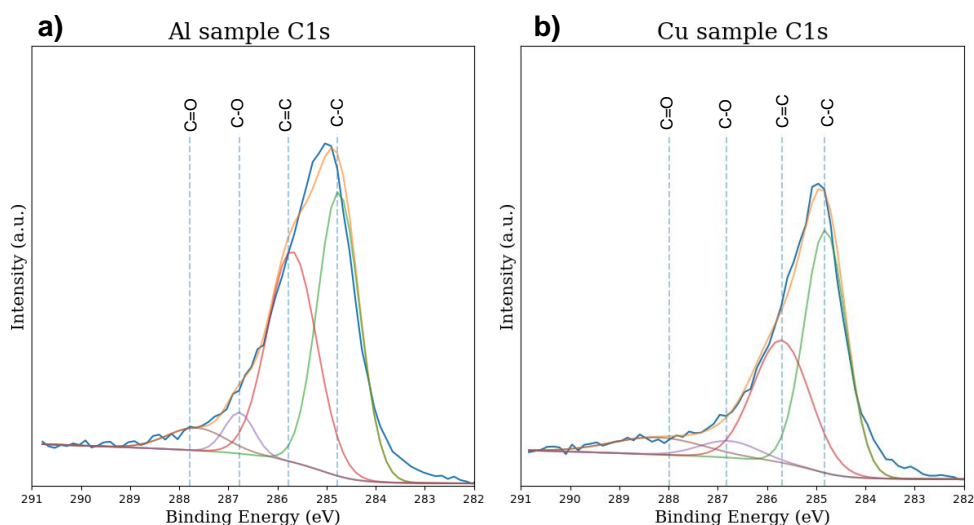


Figure 4.17: High resolution XPS C1s core level deconvoluted into main binding energy for (a) Al-CNT sample and (b) Cu-CNT sample.

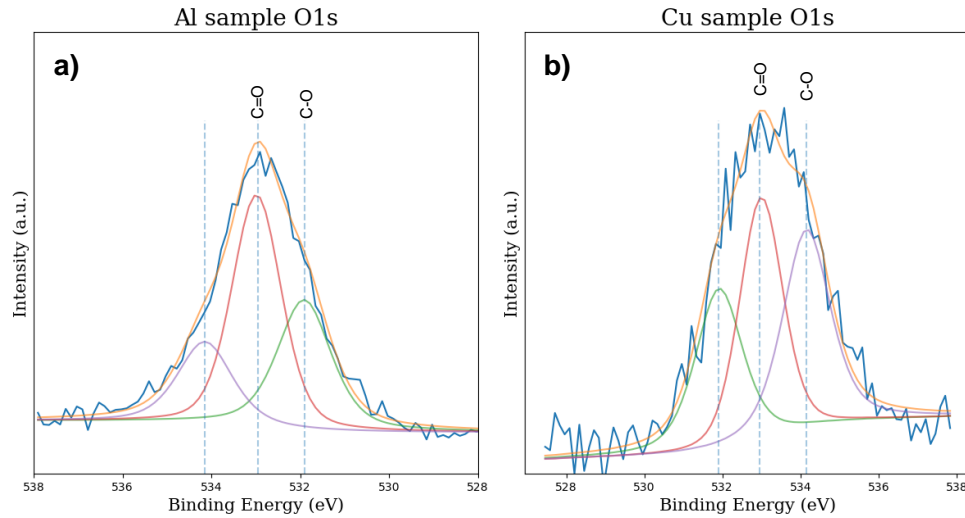


Figure 4.18: High resolution XPS O1s core level deconvoluted into main binding energy for (a) Al-CNT sample and (b) Cu-CNT sample..

4.6 Radiation capture results

This section will analyse the data collected with the device created connected to 4 different samples in order to test and compare the effectiveness of radiation capture. The materials tested are CNT-Al, CNT-Cu, a copper sample and a Aluminum sample, described in section 4.2. This test will provide us with information to determine which sample is more effective to transform solar radiation into heat. Once the data was obtained directly to a macros enabled Excel document, the graphs were created with python's matplotlib library. The studies with the Xenon lamp were made at CENCINAT in ESPE university and the solar test took place in Quito - Ecuador (-0.254428, -78.480638).

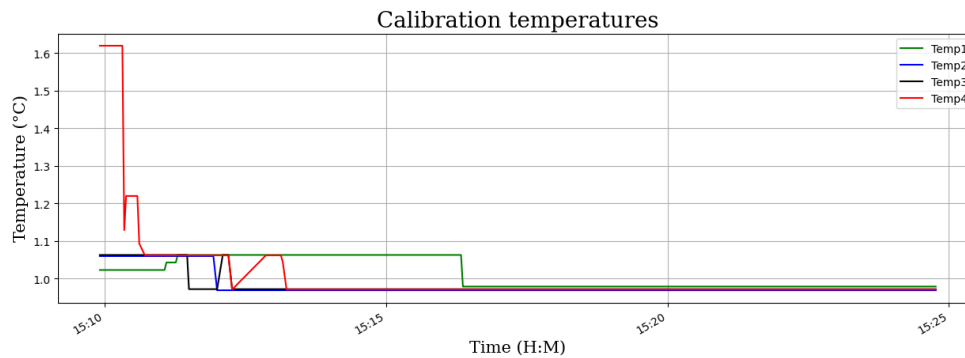


Figure 4.19: Calibration with offset and reference instruments for all the pt100 temperature sensors.

For the first test, the 4 samples were attached with thermal paste to the pt100 temperature sensors under a preheated Xenon lamp. This process was done with a room temperature of 18 °C. The test remained unaltered for 2 hours under the xenon lamp. In Figure 4.20 we can see how the samples gradually heated under the light with 427 Watts. As we can observe there is an evident difference between samples, even though the distance between the source of light and the samples is constant. After two hours the temperature increased by 8 °C for CNT-Al, followed by CNT-Cu, Cu, and lastly Al. The difference between samples is about 1 °C respectively and the temperature remained constant after the first hour of the test. The highest temperature reached was 26.48 °C with CNT-Al after two hours of exposure to the Xenon lamp. This test shows how the effectiveness of the radiation capture is greater not only between the CNT and no CNT samples, but also between the quality and crystalline structure difference of CNT-Al and CNT-Cu even at low (427 W) power exposures.

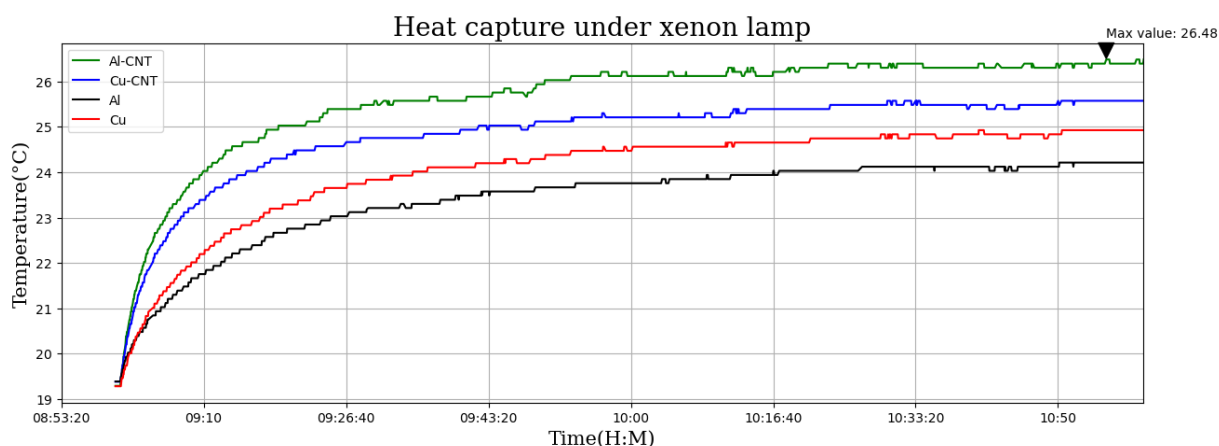


Figure 4.20: Temperature readings of the heat capture for 1)Al-CNT 2)Cu-CNT 3)Al 4)Cu under a xenon lamp.

In order to test the radiation capture under the sun certain criteria needed to be fulfilled. The hour influence in the radiation levels the sun provides, being the highest at 12:00 PM. The clouds and the humidity are a big problem to the exposure of the samples, so a relatively clear sky was needed and should remain for the entirety of the test. This proved to be obstacles in the capture of data, however the results shown in Figure 4.21, proves CNT-Al and CNT-Cu to be more effective in radiation capture by almost 8 °C and CNT-Al having the highest temperature with 37.02 °C. In this setup the mean room temperature was 21 °C, meaning a temperature difference of 17.02 °C at the highest point.

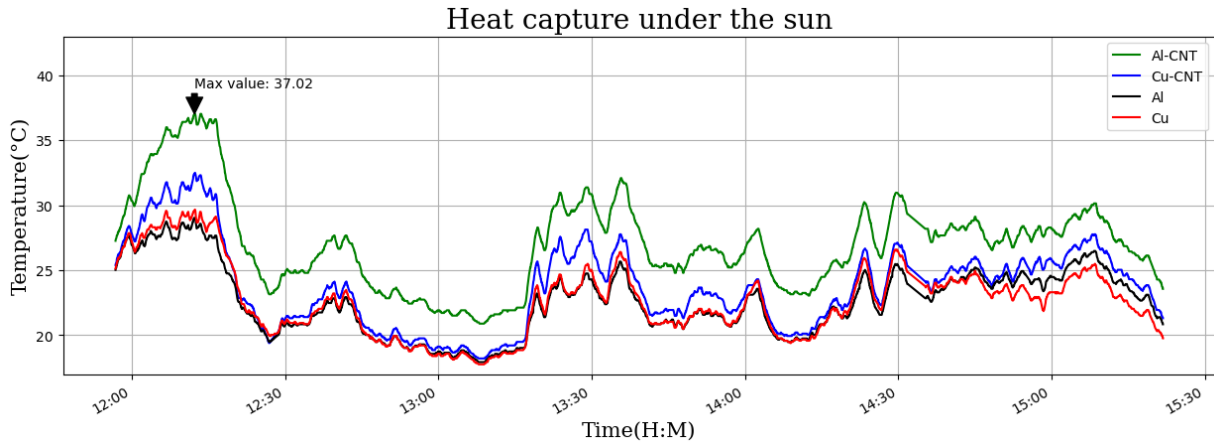


Figure 4.21: Temperature readings of the heat capture for 1) Al-CNT 2) Cu-CNT 3) Al 4) Cu under the sun.

The temperature recordings also allow us to see the effect of clouds in the drops of temperature because this setup allows the system to dissipate temperature for precise instantaneous recordings of the temperature.⁶⁷ Similar data was obtained on different test as shown in Figure 4.22, with lower temperatures and lower differences between CNT-Al and CNT-Cu, while still maintaining a mean 2 °C difference with the aluminum and copper samples.

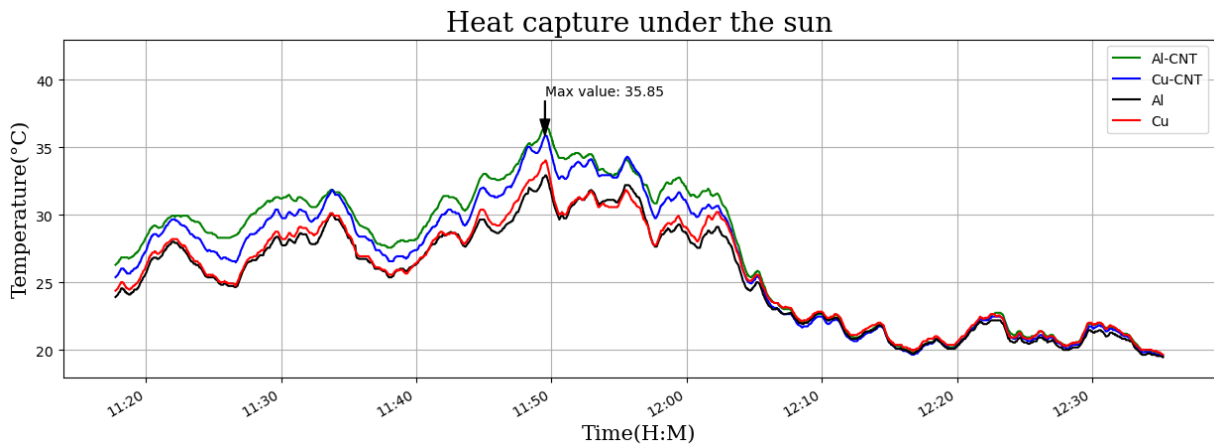


Figure 4.22: Temperature readings of the heat capture for 1) Al-CNT 2) Cu-CNT 3) Al 4) Cu under the sun.

4.7 Exergy analysis

Using equation 2.6 the exergy of the system was calculated. This calculation gives out the amount of energy that can be used for work from an specific system. The analysis of this minimum work was done with the reference of a

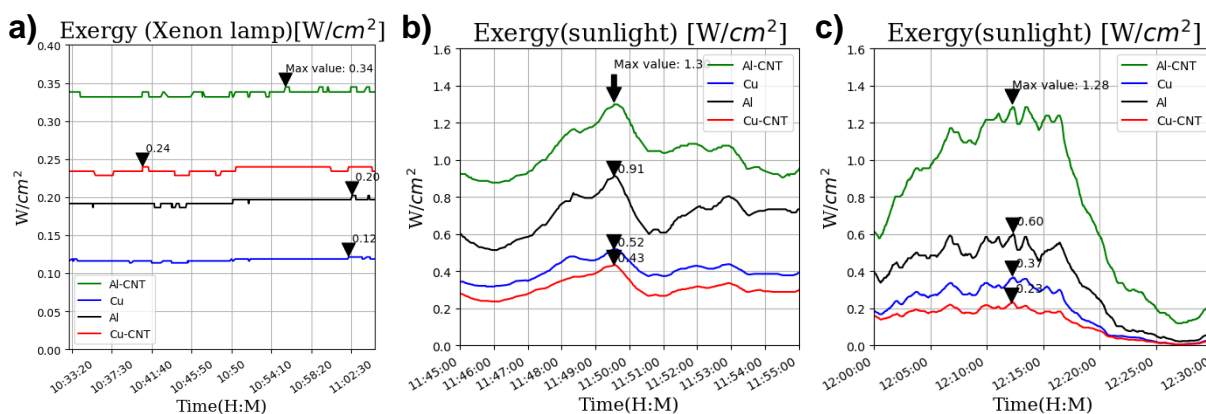


Figure 4.23: Exergy available due to difference in temperature between CNT-Al, CNT-Cu, Al and Cu samples for: (a) test under Xenon lamp (b) test under sunlight 1 (c) test under sunlight 2.

constant temperature of 18 °C which was measured with an external reference temperature instrument. By analysing the results of Section 4.5 and compare it to the exergy of the samples in Figure 4.23 we can gauge how a difference in a few degrees is important in a heating reservoir.

From Figure 4.23 part (a) we can see a difference of 0.1 W/cm² between the CNT samples, aluminum having the highest available energy under the Xenon lamp. In part (a) and (b) the difference is 0.39 and 0.68 W/cm², which shows an increase in exergy in relation to temperature, thus in radiation. Equation 2.6 allowed us to calculate exergy taking into account the heat capacity of aluminum and copper, being 0.9 J/g°C for aluminum and 0.38 J/g°C for copper. However the value was adjusted to obtain a value in relation to the exposed surface of the metal. The weight of both Al and Cu samples is 1.4 g. For Al with a thickness of 1 mm, the heat capacity is 0.225 J/cm²°C and for copper, with a thickness of 0.5 mm, is 0.095 J/cm²°C.

4.8 Luminance results.

As an addition to test the efficiency of the samples absorbing radiation, luminance was measured. This results give us a photometric measure of the intensity of the light per unit of area of light from a given direction. In this case it was used to measure the reflected light from the area of each sample. This measurements were taken only for samples under the Xenon lamp.⁶⁸ Colorimetry objective is to quantify colors with numerical values and luminance, as well as chromatic coordinates and purity can be used to establish a specific color identity⁶⁹. Thus the color black from this point of view would be the optimal object-color stimuli is related to luminous reflectance of 0, where, meaning black is the color with lower luminance and thus colorimetric purity.⁷⁰ However, CNTs are not inherently black, but its color depend on the structure, defects and chirality of the samples showing a wide variety of vibrant and opaque colors when classified in suspension by size and structure of different SWCNT.⁷⁰ Since the samples synthesized in this work didn't undergo any purification process, the film over the metallic sample would be the bulk product of

CVD-grown C-C structures. Luminance dynamics studies of individual CNTs have been developed, but due to the scale of the synthesis process, as well as the in-situ analysis of the samples, previous studies does not scale up for the size of this work.^{71 72}

The measurements where time independent, thus the values are an average of the values measured over 2 hours. For CNT-Al the value $360,83 \text{ cd/m}^2$, CNT-Cu had 376.33 cd/m^2 , Al sample had 1921.33 cd/m^2 and lastly $1919,33 \text{ cd/m}^2$. Scaling up to the size of the samples, we have that for 4 cm^2 samples, the luminous intensity in cd is 0.036, 0.037, 0.1921 and 0.1919 cd for CNT-Al, CNT-Cu, Al and Cu correspondingly. This measurement from the radiant intensity indicates that the lower value of 0.036 cd of CNT-Al is nearest to absolute black compared to the other samples.⁷¹

Chapter 5

Conclusions & Outlook

To summarize, the work done was an effort to create a material to contribute to energy absorption of green sources, thus providing an additional option for a transition to renewable and efficient energies. Using chemical vapor deposition as a synthesis technique for the in situ growth of carbon nanotubes over metallic plates we were able to evaluate its properties of converting usable solar radiation (exergy) for the industrial sector. The process is summarized as follows:

5.1 Synthesis of CNTs over surface treated aluminum and copper

Aluminum and copper sheets with a thickness of 1 mm and 0.5 mm respectively and 4 cm^2 were the starting point of the synthesis. In order to remove oxide film impurities, create a texture surface for a better and smoother catalytic coating and create a series of topological defects to increase the superficial area to create a network of CNTs that would increase the radiation absorption, a two stage surface treatment took place beginning with sonication with a NaCl solution to create nanopiramidal structures and after that rinsing the samples with ethanol. Later electrochemical etching allowed the samples to create a visible and homogeneous dispersion of holes and crevices over the metallic surface for both aluminum and copper. The samples were rinsed afterwards with ethanol for 10 min to remove any impurities over the surface. The samples were placed over a heated plate of approximate $50 \text{ }^\circ\text{C}$ for the catalyst deposition and using an airbrush to create an even coating of 0.1 molar iron (III) and 0.1 molar cobalt (II) nitrate aqueous solution and even coating was created. Lastly the samples were introduced to the CVD and heated to $750 \text{ }^\circ\text{C}$ for copper and $520 \text{ }^\circ\text{C}$ for aluminum. The reaction took place under a flow of 0.30 l/h Ar and 0.1 l/h C_2H_2 for 15 min and 20 min. The results of this process are detailed on Section 4.1.

5.2 Characterization of MWCNTs

The samples were tested with different characterization methods to verify the structural properties of the material. Raman showed the spectrum of a high crystallinity MWCNTs over aluminum with D, G and 2D band located at 1349, 1586 and 2461 cm^{-1} respectively. However, copper-CNT samples showed different structural properties under Raman spectroscopy. Characteristic D, G and 2D bands were located at 1337, 1604 and 2714 cm^{-1} . XPS analysis allowed us to visualize the chemical composition of the surface of the sample and possible contamination. The analysis showed the presence of predominant sp² and sp³ hybridization showing the structure of MWCNTs for copper and aluminum samples while also showing zinc contamination on CNT-Al surface coating. The images from Scanning Electron Microscopy (SEM) showed a variety of carbon structures. Over aluminum CNT tubular structures with a diameter ranging from 30 nm to 110 nm were observed with no specific alignment. For copper, spherical structures were prevalent, with a diameter of 0.45 μm as well as capsules with a diameter of 17.5 nm.

5.3 Radiation-thermal capture analysis.

This work tested the CNT-metal devices using a Xenon lamp and sunlight in order to measure the efficiency of the samples to capture radiation and transform it into heat. The device created used a PLC with four sensors to measure the instantaneous temperature of four samples simultaneously. In this tests the CNT-Al samples proved to be the most efficient material for the task, having an approximate 1 °C difference under the xenon lamp and 3.5 °C under sunlight over CNT-Cu samples and an even wider difference of 6.7 °C with no CNT treatment samples. In conclusion, different samples had different thermal behavior under the same amount of radiation, CNT-Al being the most effective and showing a wider difference under more intense exposure such as sunlight over the Xenon lamp. However, meteorological changes prove to be detrimental for the measurements and replicability of the tests. Further details and analysis on section 4.

5.4 Exergy of the samples

The calculation of exergy gives us the possibility to evaluate the efficiency of the samples to fulfill the objective of solar radiation collection. CNT-Al samples were the most efficient in this task, showing a difference of 0.1 W/cm^2 with CNT-Cu under Xenon lamp and up to 0.22 W/cm^2 with untreated samples. For sunlight the samples showed a greater difference (1 W/cm^2) meaning that for greater intensity, not only the temperature of the sample is higher but also its capability of giving energy. The results show as expected the quality of the samples for solar collection systems and a general outline for improvement to reach the industry.

5.5 Luminance analysis

The results obtained through the measurement of luminance can be related to a colorimetry analysis of each sample created. Because the measurement gives us information about the light reflected by the coating of the sample, a

value near 0 would mean the coating is completely absorbing. Real approximations have been obtained with CNT through vertical alignment and vertically fictionalized substrates such as black-Si^{30 62}. However, having the costs of production in mind, the treatment process gave out promising values. CNT-Al had a luminous intensity measurement of 0.036 cd on a 2x2 cm sample and that indicates not only the color of the sample but also how little light the coating reflects.

5.6 Outlook

In conclusion, the results of the synthesis where an even black coating of MWCNTs was grown using CVD. Using Raman spectroscopy, XPS and SEM we were able to identify the nanostructures grown over the samples, ensuring CNTs over the samples as well as different carbon materials produced in bulk. To test the efficiency, PLC with 4 temperature sensors provided an accurate data acquisition simultaneously and reliably. With the results of solar collector we could compare the efficiency of each material, CNT-Al being the best harvesting solar radiation and turning it into heat with a difference of 2 °C under Xenon Lamp and 4°C under sunlight in comparison to CNT-Cu, as well as showing the lowest luminous intensity 0.036 cd, the nearest sample to reach ultra black. Lastly to evaluate the possible partial transition of industry applications, the exergy of the samples showed the efficiency of each material to provide work or energy. The most efficient was CNT-Al, although having a difference of 0.1 W/cm² under Xenon lamp and 0.4 W/cm² compared to CNT-Cu. This would imply that 1 m² of this material would be able to generate 13000 W of work, being 3900 W more than CNT-Cu and 8700 more than non-CNT samples. The results establish the possibility and using more sophisticated synthesis techniques and purification of the samples, the partial transition for this type of renewable energy is promising.

Appendix A

Baseline removal

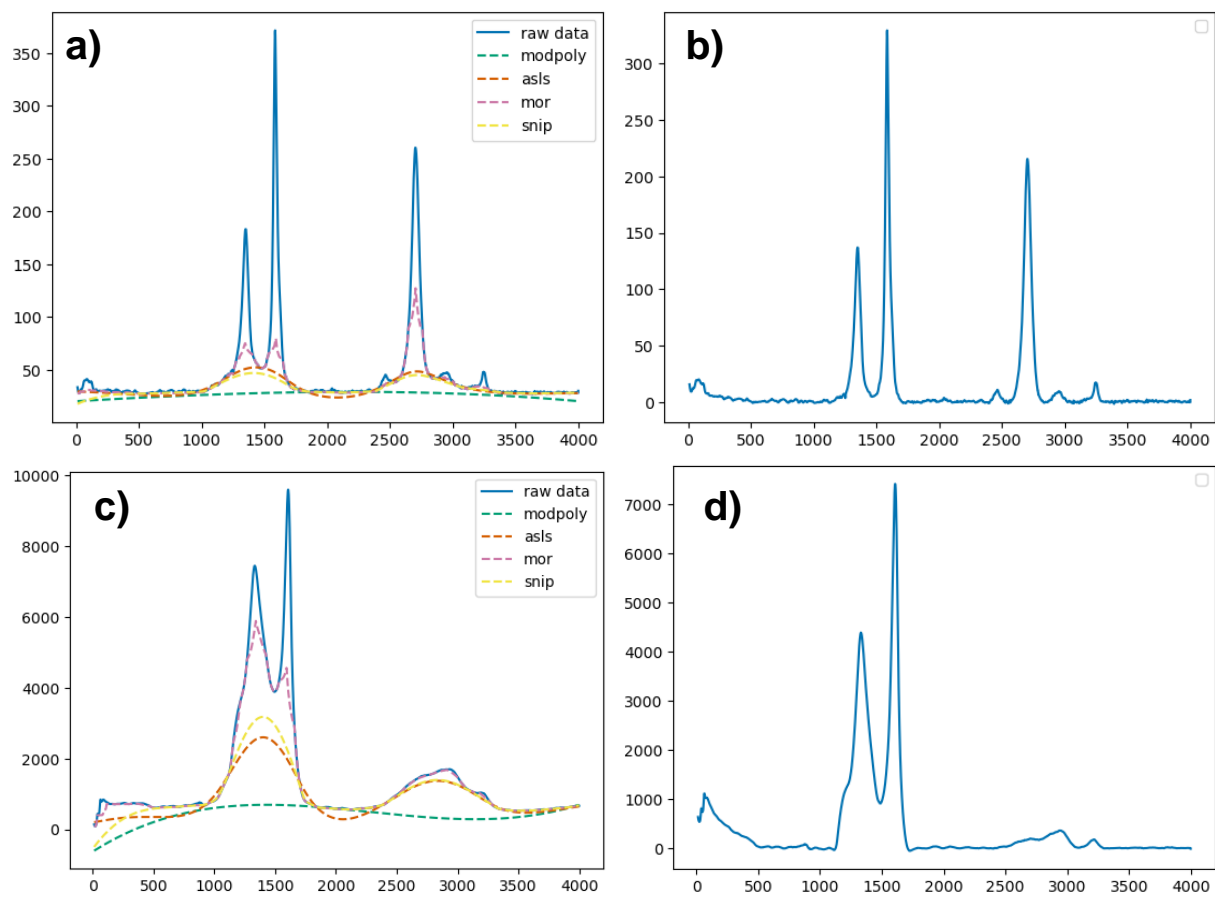


Figure A.1: Baseline removal using Baseline.py library for python. (a) shows the different baseline removals able for the spectra and (b) is the result after the removal for CNT-Al sample. (c) shows the different baseline removals able for the spectra and (d) is the result after the removal for CNT-Cu sample.

Bibliography

- [1] Vera Grunauer, X. *Balance energetico nacional 2021*; 2022.
- [2] Birol, F. Heat – renewables 2019 – analysis. 2019; <https://www.iea.org/reports/renewables-2019/heat>.
- [3] Cirocco, L.; Belusko, M.; Bruno, F.; Boland, J.; Pudney, P. Optimisation of Storage for Concentrated Solar Power Plants. *Challenges* **2014**, *5*.
- [4] Che, J.; Cagin, T.; Goddard III, W. A. Thermal conductivity of carbon nanotubes. *Nanotechnology* **2000**, *11*, 65.
- [5] Pant, M.; Singh, R.; Negi, P.; Tiwari, K.; Singh, Y. A comprehensive review on carbon nano-tube synthesis using chemical vapor deposition. *Materials Today: Proceedings* **2021**, *46*, 11250–11253, International Conference on Technological Advancements in Materials Science and Manufacturing.
- [6] Zhou, W.; Apkarian, R.; Wang, Z. L.; Joy, D. In *Scanning Microscopy for Nanotechnology: Techniques and Applications*; Zhou, W., Wang, Z. L., Eds.; Springer New York: New York, NY, 2007; pp 1–40.
- [7] Tian, Y.; Zhao, C. A review of solar collectors and thermal energy storage in solar thermal applications. *Applied Energy* **2013**, *104*, 538–553.
- [8] Terranova, M.; Sessa, V.; Rossi, M. The World of Carbon Nanotubes: An Overview of CVD Growth Methodologies. *Chemical Vapor Deposition* **2006**, *12*, 315–325.
- [9] Shu-Cheng, Y.; Hon-Sho, C.; Fon-Shu, G. Effects of substrate pretreatment on the growth of diamond films with CVD method. *Journal of Crystal Growth* **1990**, *99*, 1196–1200.
- [10] Dresselhaus, M.; Dresselhaus, G.; Saito, R.; Jorio, A. Raman spectroscopy of carbon nanotubes. *Physics Reports* **2005**, *409*, 47–99.
- [11] Saidur, R.; Atabani, A.; Mekhilef, S. A review on electrical and thermal energy for industries. *Renewable and Sustainable Energy Reviews* **2011**, *15*, 2073–2086.

- [12] Farjana, S. H.; Huda, N.; Mahmud, M. P.; Saidur, R. Solar process heat in industrial systems – A global review. *Renewable and Sustainable Energy Reviews* **2018**, *82*, 2270–2286.
- [13] McMillan, C.; Broadman, R.; McKellar, M.; Sabharwal, P.; Ruth, M.; Bragg-Sitton, S. *Generation and Use of Thermal Energy in the U.S. Industrial Sector and Opportunities to Reduce its Carbon Emissions*; 2016; p 3–191.
- [14] Midilli, A.; Dincer, I.; Ay, M. Green energy strategies for sustainable development. *Energy policy* **2006**, *34*, 3623–3633.
- [15] Isravel, R. S.; Saravanan, S.; Vijayan, V. A review of material and coatings in solar collectors. *Materials Today: Proceedings* **2020**, *21*, 497–499, International Conference on Recent Trends in Nanomaterials for Energy, Environmental and Engineering Applications.
- [16] Iijima, S. Helical microtubules of Graphitic Carbon. *Nature* **1991**, *354*, 56–58.
- [17] Khiriya, P. K.; Chauhan, J. Theoretical Studies of Single Wall Carbon Nanotubes for Synthesis and Growth Mechanism.
- [18] Eatemadi, A.; Daraee, H.; Karimkhanloo, H.; Kouhi, M.; Zarghami, N.; Akbarzadeh, A.; Abasi, M.; Hanifehpour, Y.; Joo, S. W. Carbon nanotubes: properties, synthesis, purification, and medical applications. *Nanoscale research letters* **2014**, *9*, 1–13.
- [19] Khanna, V.; Kumar, V.; Bansal, S. A. Mechanical properties of aluminium-graphene/carbon nanotubes (CNTs) metal matrix composites: Advancement, opportunities and perspective. *Materials Research Bulletin* **2021**, *138*, 111224.
- [20] Georgakilas, V.; Perman, J. A.; Tucek, J.; Zboril, R. Broad Family of Carbon Nanoallotropes: Classification, Chemistry, and Applications of Fullerenes, Carbon Dots, Nanotubes, Graphene, Nanodiamonds, and Combined Superstructures. *Chemical Reviews* **2015**, *115*, 4744–4822, PMID: 26012488.
- [21] Manocha, L. Introduction of nanostructures in carbon–carbon composites. *Materials Science and Engineering: A* **2005**, *412*, 27–30.
- [22] Du, R.; Ssenyange, S.; Aktary, M.; McDermott, M. T. Fabrication and characterization of graphitic carbon nanostructures with controllable size, shape, and position. *Small* **2009**, *5*, 1162–1168.
- [23] Lin, Y.-C.; Lin, J.-H. Purity-controllable growth of bamboo-like multi-walled carbon nanotubes over copper-based catalysts. *Catalysis Communications* **2013**, *34*, 41–44.
- [24] Keszler, A.; Nemes, L.; Ahmada, S.; Fanga, X. Characterisation of carbon nanotube materials by Raman spectroscopy and microscopy - A case study of multiwalled and singlewalled samples. **2004**, *6*.
- [25] Pan, H.; Feng, Y.; Lin, J. Ab initio study of electronic and optical properties of multiwall carbon nanotube structures made up of a single rolled-up graphite sheet. *Physical Review B* **2005**, *72*, 085415.

- [26] Wong, C. H. A.; Pumera, M. Unscrolling of multi-walled carbon nanotubes: towards micrometre-scale graphene oxide sheets. *Physical Chemistry Chemical Physics* **2013**, *15*, 7755–7759.
- [27] Liu, Z.-Q.; Ma, J.; Cui, Y.-H.; Zhang, B.-P. Effect of ozonation pretreatment on the surface properties and catalytic activity of multi-walled carbon nanotube. *Applied Catalysis B: Environmental* **2009**, *92*, 301–306.
- [28] Stephens, M. S.; Simonds, B. J.; Yung, C. S.; Conklin, D.; Livigni, D. J.; Oliva, A. R.; Lehman, J. H. Reduction of short wavelength reflectance of multi-wall carbon nanotubes through ultraviolet laser irradiation. *AIP Advances* **2018**, *8*.
- [29] Wang, X.; Wang, L.; Adewuyi, O.; Cola, B. A.; Zhang, Z. Highly specular carbon nanotube absorbers. *Applied Physics Letters* **2010**, *97*.
- [30] Wang, X.; Flicker, J.; Lee, B. J.; Ready, W.; Zhang, Z. Visible and near-infrared radiative properties of vertically aligned multi-walled carbon nanotubes. *Nanotechnology* **2009**, *20*, 215704.
- [31] Shimizu, Y.; Ishii, J. Blackbody thermal radiator with vertically aligned carbon nanotube coating. *Japanese Journal of Applied Physics* **2014**, *53*, 068004.
- [32] Fleming, J. C.; Collins, S.; Kelsic, Carbon Nanotube Flat Plate Blackbody Calibrator. **2017**,
- [33] Yang, Z.-P.; Ci, L.; Bur, J. A.; Lin, S.-Y.; Ajayan, P. M. Experimental Observation of an Extremely Dark Material Made By a Low-Density Nanotube Array. *Nano Letters* **2008**, *8*, 446–451, PMID: 18181658.
- [34] Kumaneck, B.; Janas, D. Thermal conductivity of carbon nanotube networks: A review. *Journal of materials science* **2019**, *54*, 7397–7427.
- [35] Han, Z.; Fina, A. Thermal conductivity of carbon nanotubes and their polymer nanocomposites: A review. *Progress in polymer science* **2011**, *36*, 914–944.
- [36] Kwon, Y.-K.; Kim, P. Unusually high thermal conductivity in carbon nanotubes. *High Thermal Conductivity Materials* **2006**, 227–265.
- [37] Wang, P.; Xiang, R.; Maruyama, S. Thermal conductivity of carbon nanotubes and assemblies. *Advances in Heat Transfer* **2018**, *50*, 43–122.
- [38] Zhang, Q.; Chen, G.; Yoon, S.; Ahn, J.; Wang, S.; Zhou, Q.; Wang, Q.; Li, J. Thermal conductivity of multiwalled carbon nanotubes. *Physical Review B* **2002**, *66*, 165440.
- [39] Ghalandari, M.; Maleki, A.; Haghighi, A.; Shadloo, M. S.; Nazari, M. A.; Tlili, I. Applications of nanofluids containing carbon nanotubes in solar energy systems: A review. *Journal of Molecular Liquids* **2020**, *313*, 113476.

- [40] Jamil, M. M.; Sidik, N. A. C.; Umar, U. S.; Hamisu, M. T.; Sa'ad, A. Carbon nanotube for solar energy applications: A review. *Journal of Advanced Research in Fluid Mechanics and Thermal Sciences* **2019**, *56*, 233–247.
- [41] Moran, M.; Sciubba, E. Exergy analysis: principles and practice. **1994**,
- [42] Koroneos, C.; Spachos, T.; Moussiopoulos, N. Exergy analysis of renewable energy sources. *Renewable energy* **2003**, *28*, 295–310.
- [43] Alberto, R. J. C.; Alexander, H. S. A. Conversion of solar radiation into heat through carbon nanotubes with potential industrial applications. Ph.D. thesis, School of physical sciences and nanotechnology, 2022.
- [44] Li, X.; Baker-Fales, M.; Almkhelfe, H.; Gaede, N. R.; Harris, T. S.; Amama, P. B. Rational modification of a metallic substrate for CVD growth of carbon nanotubes. *Scientific Reports* **2018**, *8*.
- [45] Alwarappan, S.; Prabhulkar, S.; Durygin, A.; Li, C.-Z. The effect of electrochemical pretreatment on the sensing performance of single walled carbon nanotubes. *Journal of nanoscience and nanotechnology* **2009**, *9*, 2991–2996.
- [46] Phan, T. L.; Yu, W. J. CVD-grown carbon nanotube branches on black silicon stems for ultrahigh absorbance in wide wavelength range. *Scientific Reports* **2020**, *10*.
- [47] Cui, K.; Wardle, B. L. Breakdown of native oxide enables multifunctional, free-form carbon nanotube–metal hierarchical architectures. *ACS applied materials & interfaces* **2019**, *11*, 35212–35220.
- [48] Quinton, B. T.; Leedy, K. D.; Lawson, J. W.; Tsao, B.; Scofield, J. D.; Merrett, J. N.; Zhang, Q.; Yost, K.; Mukhopadhyay, S. M. Influence of oxide buffer layers on the growth of carbon nanotube arrays on carbon substrates. *Carbon* **2015**, *87*, 175–185.
- [49] Xiao, P.; feng Lu, X.; Liu, Y.; He, L. Effect of in situ grown carbon nanotubes on the structure and mechanical properties of unidirectional carbon/carbon composites. *Materials Science and Engineering: A* **2011**, *528*, 3056–3061.
- [50] Ferraro, J. R. *Introductory raman spectroscopy*; Elsevier, 2003.
- [51] Smith, E.; Dent, G. *Modern Raman spectroscopy: a practical approach*; John Wiley & Sons, 2019.
- [52] Long, D. A. Raman spectroscopy. *New York* **1977**, *1*.
- [53] Mohammed, A.; Abdullah, A. Scanning electron microscopy (SEM): A review. **2018**, *2018*, 7–9.
- [54] Li, W.; Bauhofer, W. Imaging of CNTs in a polymer matrix at low accelerating voltages using a SEM. *Carbon* **2011**, *49*, 3891–3898.
- [55] Zipperian, D. C. *METALLOGRAPHIC HANDBOOK*; PACE Technologies, USA, 2011.

- [56] Park, D.; KIM, H. Electrochemical etching of aluminum through porous alumina. *Analytical Sciences/Supplements* **2001**, *17*, a73–a76.
- [57] Cao, Z.; Sun, Z.; Guo, P.; Chen, Y. Effect of acetylene flow rate on morphology and structure of carbon nanotube thick films grown by thermal chemical vapor deposition. *Frontiers of Materials Science in China* **2007**, *1*, 92–96.
- [58] Blackburn, J. L. Semiconducting single-walled carbon nanotubes in solar energy harvesting. *ACS Energy Letters* **2017**, *2*, 1598–1613.
- [59] Said, Z.; Saidur, R.; Sabiha, M.; Rahim, N.; Anisur, M. Thermophysical properties of Single Wall Carbon Nanotubes and its effect on exergy efficiency of a flat plate solar collector. *Solar Energy* **2015**, *115*, 757–769.
- [60] Kondo, K.; Kurihara, H.; Murakami, H. Etching morphology of single-crystal copper. *Electrochemical and solid-state letters* **2005**, *9*, C36.
- [61] Sun, L.; Yuan, G.; Gao, L.; Yang, J.; Chhowalla, M.; Gharahcheshmeh, M. H.; Gleason, K. K.; Choi, Y. S.; Hong, B. H.; Liu, Z. Chemical vapour deposition. *Nature Reviews Methods Primers* **2021**, *1*.
- [62] De Nicola, F.; Hines, P.; De Crescenzi, M.; Motta, N. Thin randomly aligned hierarchical carbon nanotube arrays as ultrablack metamaterials. *Phys. Rev. B* **2017**, *96*, 045409.
- [63] Ferrari, A. C.; Robertson, J. Interpretation of Raman spectra of disordered and amorphous carbon. *Phys. Rev. B* **2000**, *61*, 14095–14107.
- [64] Costa, S.; Borowiak-Palen, E.; Kruszynska, M.; Bachmatiuk, A.; Kalenczuk, R. Characterization of carbon nanotubes by Raman spectroscopy. *Materials Science-Poland* **2008**, *26*, 433–441.
- [65] XPS, T. S. *Carbon*; 2021.
- [66] XPS, T. S. *Oxygen*; 2021.
- [67] Mahbulul, I.; Khan, M. M. A.; Ibrahim, N. I.; Ali, H. M.; Al-Sulaiman, F. A.; Saidur, R. Carbon nanotube nanofluid in enhancing the efficiency of evacuated tube solar collector. *Renewable energy* **2018**, *121*, 36–44.
- [68] Lennie, P.; Pokorny, J.; Smith, V. C. Luminance. *JOSA A* **1993**, *10*, 1283–1293.
- [69] Pridmore, R. W. Chromatic luminance, colorimetric purity, and optimal aperture-color stimuli. *Color Research & Application* **2007**, *32*, 469–476.
- [70] Wei, N.; Tian, Y.; Liao, Y.; Komatsu, N.; Gao, W.; Lyuleeva-Husemann, A.; Zhang, Q.; Hussain, A.; Ding, E.-X.; Yao, F. Colors of single-wall carbon nanotubes. *Advanced Materials* **2021**, *33*, 2006395.
- [71] Berciaud, S.; Cognet, L.; Lounis, B. Luminescence Decay and the Absorption Cross Section of Individual Single-Walled Carbon Nanotubes. *Phys. Rev. Lett.* **2008**, *101*, 077402.

- [72] Mantiuk, R.; Daly, S.; Kerofsky, L. The luminance of pure black: exploring the effect of surround in the context of electronic displays. **2010**, *7527*, 264–271.